Science
AAAS

Supplementary Materials for

Emergent ferroelectricity in subnanometer binary oxide films on silicon

Suraj S. Cheema *et al*.

Corresponding authors: Suraj S. Cheema, s.cheema@berkeley.edu; Sayeef Salahuddin, sayeef@berkeley.edu

Science **376**, 648 (2022)
DOI: 10.1126/science.abm8642

The PDF file includes:

Materials and Methods

Synthesis and Processing

All thin film synthesis was performed at U.C. Berkeley; all device processing was performed at the U.C. Berkeley Marvell Nanofabrication Laboratory.

Film deposition Thin films of ZrO_2 were grown by atomic layer deposition (ALD) in a Fiji Ultratech/Cambridge Nanotech tool at 300°C in which tetrakis (ethylmethylamino) zirconium precursors are heated to 75°C and water vapor is used as the oxidant. The ALD growth technique facilitates atomic-level thickness control and conformal deposition for highly-scaled semiconductor applications (*35*). For metal-ferroelectric-insulator-semiconductor (MFIS) capacitor structures, 1 nm chemically-grown SiO_2 on Si was prepared by the standard clean (SC-1) solution (5:1:1 H_2O:H_2O_2:NH_4OH at 80°C for 10 minutes) after the Si wafer was cleaned in Piranha (120°C for 10 minutes) to remove organics and HF (50:1 H_2O:HF at room temperature for 30 s) to remove any native oxide. For interdigitated electrode (IDE) structures, 100 nm of SiO_2 is grown by thermal oxidation on Si. For metal-insulator-metal (MIM) capacitor structures, the bottom metal (TiN) is deposited by sputtering at room temperature on Si. Subsequently, ZrO_2 is deposited at 300°C by ALD in which 10 ALD cycles corresponds to one nanometer of ZrO_2 film, as confirmed by X-ray reflectivity and out-of-plane grain size analysis (fig. S1). Finally, for MFIS and MFM structures, the top metal (TiN and/or W) is deposited by sputtering at room temperature. For bare ferroelectric films (structural and optical studies), the top metal is not deposited.

Capacitor fabrication For MFIS and MFM capacitor structures (*P-V*, *C-V* and *I-V* characterization), micron-sized top electrodes of various areas are defined by photolithography and selective etching of the top TiN and/or W metal layer.

Interdigitated electrode fabrication For in-plane interdigitated electrode (IDE) device structures, 1-5 μm spaced IDEs are patterned by lift-off photolithography on bare ZrO_2 films grown on 100 nm of thermal SiO_2. The metal electrodes (Ti(5 nm)/Au(120 nm)) are then deposited with e-beam evaporation.

Transmission Electron Microscopy

HR-TEM Electron microscopy was performed at the National Center for Electron Microscopy (NCEM) facility of the Molecular Foundry at Lawrence Berkeley National Laboratory (LBNL). High-resolution transmission electron microscopy (HR-TEM) images of 5 nm and 2 nm ZrO_2 were performed by aberration-corrected FEI ThemIS 60-300 STEM/TEM microscope operated at 300 kV using a TEM mode for atomic scale imaging. In order to precisely identify the fluorite-structure in ultrathin ZrO_2 films, the NCSI technique was employed to probe not only the zirconium sublattice, but also the oxygen sublattice. The cross-sectional TEM samples of 5 nm and 2 nm ZrO_2 were mechanically polished using an Allied High Tech Multiprep at a 0.5° wedge. After thinning the total thickness of samples down to 10 μm, the specimens were Ar ion milled using a Gatan Precision Ion Milling System to an electron-transparent specimen starting from 4 keV down to 200 eV as the final cleaning energy.

NCSI and HR-TEM Simulations For the NCSI technique, the oxygen atoms are expected to be visible for specimen thicknesses below ~ 10 nm (*36*); therefore, the experimental HR-TEM data was acquired at similarly thin specimen thicknesses. From HR-TEM imaging, the oxygen atoms became apparent under the following experimental conditions: tuning the defocus (C_1) at spherical aberration (C_s) values of C_3 = -16 μm and C_5 = 6.8 mm. The HR-TEM image simulations were calculated using the Prismatic method (*37,38*) under the specified experimental conditions. After tuning the defocus (~ 2 to 4 nm) in tandem with the slice thickness (~ 20 Å) and specimen thickness (below 12.5 nm) (fig. S6), the oxygen atoms were clearly visible within the zirconium sublattice. In general, the grain size along the beam direction is comparable to the grain width parallel to the interface for the same image, which is ~ 5-15 nm (fig. S3); therefore, it is reasonable for the specimen thickness to range around the ZrO_2 grain size. Based on these experiment-guided conditions, the HR-TEM simulations for the tetragonal $P4_2/nmc$ (specimen thickness = 9.8 nm and defocus = 4 nm) and orthorhombic $Pca2_1$ (specimen thickness = 9.81 nm and defocus = 4 nm) were found to match well with the experimental data for 5 nm and 2 nm ZrO_2 films, respectively (Fig. 1E,G).

HAADF-STEM Wide field-of-view and local imaging of 5 ALD cycle (~ 0.5 nm) ZrO_2 thin films were performed by high-angle annular dark-field scanning transmission electron microscopy (HAADF-STEM) at 300kV to confirm the wide-area stability and thickness of ultrathin ZrO_2, respectively (fig. S2). The ultrathin ZrO_2 layer was surrounded by high contrast neighboring layers (low-Z SiO_2 underlayer and low-Z Al_2O_3 capping layer) to aid in layer delineation.

Scanning Probe Microscopy

Atomic force microscopy (AFM) and piezoresponse force microscopy (PFM) measurements were performed using a commercial scanning probe microscope (Asylum MFP-3D) at UC Berkeley. Dual-frequency resonance-tracking PFM (*39*) was conducted using a conductive Pt/Ir-coated probe tip (NanoSensor PPP-EFM) to measure switching-spectroscopy (SS) (*40*) piezoresponse hysteresis loops (fig. S14C) and image written domain structures (fig. S13). Resonance-enhanced PFM increases the signal to noise ratio for the detection of out-of-plane electric polarization, critical for ultrathin films. Contact was made to the bottom TiN electrode or heavily doped Si electrode for all PFM studies. For bare imaging studies, contact was made to the bare ZrO_2 surface. Switching spectroscopy hysteresis loops were measured on capacitor structures to help eliminate electrostatic artifacts from the tip (*41*), mitigate possible electromechanical contributions (*42*), and to yield more confined electric fields.

Optical Characterization

The second harmonic generation (SHG) measurement geometries are sensitive to in-plane inversion symmetry breaking in the ferroelectric ZrO_2 thin films (see Supplementary Text section “SHG sensitivity to in-plane polarization”).

SHG mapping Second harmonic generation (SHG) spatial mapping measurements (Fig. 2C) were performed with a Ti:sapphire femtosecond laser (Tsunami, Spectra Physics, λ ~ 800 nm, frequency ~ 80 MHz). The linearly polarized femtosecond laser beam was focused through 50X objective lens (NA ~ 0.42) which results in a focal spot size of 2 μm. The generated SHG signal was collected through the same objective lens and separated from the fundamental beam by the

harmonic separator. After passing through the optical bandpass filter, the SHG signals were registered to the photon multiplier tube (PMT) without a polarizer. The fundamental beam was mechanically chopped, and the signal collected by the PMT was filtered by a lock-in amplifier to reduce the background noise. For SHG spatial mapping, a two-axis piezo stage was utilized and the coordinate was synchronized with the PMT signal (fig. S12A). The SHG intensity was obtained by averaging the mapping signals across a 100 μm × 100 μm sample area.

SHG spectrum For SHG emission spectrum measurement, the optical beam path was the same as the setup for SHG mapping, except for the laser wavelength, optical filter, and photon detection components (fig. S12B). SHG spectrum measurements were performed with a Ti:sapphire femtosecond laser with 810 nm of wavelength (Tsunami, Spectra Physics, f ~ 80 MHz, pulse duration ~100 fs). The generated SHG signal was collected by a spectrometer (PI Max, Princeton Instrument) without signal demodulation after filtering by a 700 nm short-pass filter to block the fundamental laser beam at 810 nm.

X-ray Characterization

Accounting for different X-ray wavelengths XRR, OOP-GiD, and IP-GiD data is plotted in terms of Q (1/Å) rather than 2θ (°) such that X-ray data measured at various synchrotron beamlines are plotted on a consistent scale, where Q is defined as

$$Q = \frac{4\pi}{\lambda}\sin\frac{2\theta}{2}$$

where 2θ refers to the detector angle at a given X-ray wavelength λ, which varies across the different synchrotron measurement setups.

X-ray reflectivity Synchrotron X-ray reflectivity (XRR) – performed at Sector 33-BM-C beamline of the Advanced Photon Source, Argonne National Laboratory and at Beamline 2-1 of the Stanford Synchrotron Radiation Lightsource, SLAC National Accelerator Laboratory – confirmed the thickness of ultrathin ZrO_2 films (fig. S1A). Fitting analysis (fig. S1B) was performed with the python package GenX (*43*).

Grazing incidence diffraction: out-of-plane Synchrotron out-of-plane grazing-incidence diffraction (GID) was performed at Beamline 2-1 of the Stanford Synchrotron Radiation Lightsource, SLAC National Accelerator Laboratory with grazing angles $\theta < 0.2^{\circ}$ (fig. S1C). The X-ray source was fixed at 17 keV (λ = 0.729 Å). The high flux from the synchrotron source enabled collection of sufficient diffraction intensity from the few crystallographic planes present in ultrathin ZrO_2 films.

Grazing incidence diffraction: in-plane Synchrotron in-plane grazing-incidence diffraction (GID) (Fig. 1B, fig. S4) was performed at Sector 33-ID-D beamline of the Advanced Photon Source, Argonne National Laboratory. A Pilatus-II 100K Area Detector mounted on the del-arm was used to collect diffraction signal with a grazing incidence geometry. The region-of-interest on the detector was set such that the ring-like signal was fully integrated. In-plane GID was collected by sweeping the in-plane angle v (8-50°) with a fixed out-of-plane grazing angle δ (δ = 0.9°); the corrected Bragg angle (2θ) over which the data is plotted and indexed is determined from the relationship $\cos(2\theta) = \cos(v)\cdot\cos(\delta)$ set by the geometry of the diffractometer. The X-

ray source was fixed at 16 keV (λ = 0.775 Å). In-plane diffraction yields more diffraction peaks with better defined width, likely due to the preferred orientation and disc-shape domains in the film. Therefore, in-plane GID enables clear indexing to the ferroelectric orthorhombic ($Pca2_1$) and antiferroelectric tetragonal ($P4_2/nmc$) fluorite structure in the ultrathin HfO_2-ZrO_2 films, as the presence of many reflections from the in-plane GID spectra (fig. S4) allow for clear distinction from other nonpolar fluorite-structure polymorphs. Such diffraction spectra would be otherwise prohibited in typical out-of-plane geometry due to the lack of vertical diffraction planes and the large linewidth inherent to ultrathin films.

Two-dimensional diffraction Two-dimensional reciprocal space maps (fig. S3C-F) were measured at Beamline 11-3 of the Stanford Synchrotron Radiation Lightsource, SLAC National Accelerator Laboratory. Rayonix MX225 CCD area detector collected diffraction flux in the grazing incidence (θ < 0.20°) geometry; the X-ray source (50 microns vertical x 150 microns horizontal beam size) was fixed at 12.7 keV. The sample-detector work distance was set to 80 mm to enable detection of a wide region of reciprocal space (Q-range 0.2 to 5 Å) at the expense of reciprocal space resolution, set by the pixel size. The two-dimensional diffraction scans – in which a wide portion of the entire reciprocal space was collected simultaneously, rather than at discrete regions in Q_x-Q_y space – were averaged over data collection time and for repeated scans. These measurement features, in tandem with the high X-ray flux afforded by the synchrotron source, enabled sufficient diffraction signal detection and contrast in films just 1 nm in thickness. Data analysis was performed Nika, an Igor Pro package for correction, calibration and reduction of two-dimensional areal maps into one-dimensional data (*44*). Two-dimensional reciprocal space maps on bare ZrO_2 heterostructures confirm the presence of crystalline ultrathin films despite the low deposition temperature, afforded by the low crystallization temperature of ZrO_2 on Si (*45*).

X-ray absorption spectroscopy and X-ray linear dichroism Hard and soft synchrotron Xray spectroscopy (Fig. 2B, fig. S8) was measured at beamline 4-ID-D of the Advanced Photon Source, Argonne National Laboratory and Beamline 4.0.2. of the Advanced Light Source, Lawrence Berkeley National Laboratory, respectively. Spectroscopy measurements were taken at the oxygen K-edge (520-550 eV), zirconium $M_{3,2}$-edge (325-355 eV) and zirconium $L_{3,2}$-edge (2200-2350 eV). X-rays were incident at 20° off grazing. XAS (XLD) was obtained from the average (difference) of horizontal and vertical linearly polarized X-rays. To eliminate systematic artifacts in the signal that drift with time, spectra measured at ALS were captured with the order of polarization rotation reversed (e.g., horizontal, vertical, vertical, and horizontal) in successive scans, in which an elliptically polarizing undulator tuned the polarization and photon energy of the synchrotron X-ray source (*46*). Spectra measured at APS were recorded under various modes: total electron yield (TEY), fluorescence yield (FY), and reflectivity (REF).

Dielectric and electrical measurements

Metal-oxide-semiconductor (MOS) capacitance Capacitance-voltage (C-V) measurements (fig. S9) were performed using a commercial Semiconductor Device Analyzer (Agilent B1500) with a multi-frequency capacitance measuring unit (MFCMU). 19 micron W tips (d.c.P-HTR 154001, FormFactor) made electrical contact within a commercial probe station (Cascade Microtech); voltage was applied to the top electrode and the lightly-doped Si bottom electrode

was grounded. To eliminate contributions from series and parallel parasitic resistances, frequency-dependent *C-V* measurements were performed. In particular, *C-V* data was analyzed at two frequencies (100 kHz-1 MHz) to allow for the extraction of accurate frequency-independent *C-V* via a three-element circuit model consisting of the capacitor and the series and parallel resistors (*47*). The frequency-independent capacitance is given by,

$$C = \frac{f_1^2 C_1(1 + D_1^2) - f_2^2(1 + D_2^2)}{f_1^2 - f_2^2}$$

where C_i and D_i refer to the measured capacitance in parallel mode (C_p-R_p) and dissipation values at frequency f_i. The dissipation factor is given by $D = -\cot(\theta)$, where θ is the phase angle. In order to maximize the accuracy of this method, it is important the dissipation factors are small ($\ll 1$) at the frequencies chosen; therefore, high frequencies (100 kHz-1 MHz) were selected.

Metal-insulator-metal (MIM) polarization Polarization-voltage (*P-V*) measurements on MIM capacitors (Fig. 3A) were performed using a Agilent 81150A Pulse Function Arbitrary Noise Generator/InfiniiVision DSOX3024A oscilloscope setup. 19 micron W tips (d.c.P-HTR 154001, FormFactor) made electrical contact within a commercial probe station (Cascade Microtech); voltage was applied to the top electrode and the bottom TiN electrode was grounded. A bipolar triangular waveform was applied at frequencies ~ 10 kHz to obtain *P-V* loops for relatively thick (5, 10 nm) antiferroelectric ZrO_2 films (Fig. 3B).

Interdigitated electrode (IDE) polarization Polarization-voltage (*P-V*) measurements on IDE structures (Fig. 3D) were performed using a Radiant ferroelectric tester, which enables the application of high voltages (up to 100 V) required to measure micron-spaced IDE devices. A bipolar triangular waveform was applied at frequencies ~10 kHz to obtain *P-V* loops for relatively thick antiferroelectric ZrO_2 and ultrathin ferroelectric ZrO_2 films (Fig. 3E,F, fig. S10). In-plane *P-V* loops were measured on ZrO_2 samples deposited on thick (100 nm) SiO_2-buffered Si to minimize parasitic capacitance contributions from the underlying Si substrate.

Temperature-dependent polarization In-plane *P-V* loops were measured for 0.5 nm ZrO_2 IDE structures as a function of temperature (fig. S15) using a Neocera heating stage attached to a probe station equipped with a Radiant ferroelectric tester. The IDE sample was pasted to thermally-conductive, electrically-insulating AlN to eliminate charge contributions from the heating coils during *P-V* measurements. *P-V* loops were collected ranging from 25°C to 175°C in 25°C increments across 60 V bipolar hysteresis sweeps.

Metal-ferroelectric-insulator-semiconductor (MFIS) pulsed *I-V* measurements Pulsed tunnel current measurements were performed on MFIS capacitors (Fig. 3A) using a commercial Semiconductor Device Analyzer (Agilent B1500). Pulsed $I\text{-}V_{write}$ hysteresis maps (Fig. 3C, fig. S14D) were constructed using an arbitrary linear waveform generator (ALWG) to apply write voltages with progressively different amplitudes, followed by a read pulse at 200 mV (fig. 14B). Voltage was applied to the top electrode and the heavily-doped Si bottom electrode was grounded (fig. 14A).

Supplementary Text

Thickness Analysis

Local and global probes At the ultrathin thickness regime, the global nature of X-ray analysis can lead to more representative thickness determination than the local nature of TEM. In particular, X-rays at the grazing angles of θ = 0.1-0.2° employed for XRR and GiD studies (fig. S1) have a sample footprint over 50 mm for the 200 μm X-ray spot sizes used at the respective synchrotron beamlines. Considering the sample sizes used for synchrotron X-ray studies were ~ 25 mm long (cut from 6" wafers), the entire sample area, along the beam direction, was covered by the grazing incident X-rays. Meanwhile, TEM images only probe ~ hundreds of nanometers in its widest field-of-view (fig. S2A). Therefore, the global-nature of the grazing-angle X-ray measurements probes orders of magnitude larger sample area, enabling a more representative determination of the thickness.

Wide area uniformity ALD is renowned for its wafer-scale uniformity and angstrom-level thickness precision derived from its self-limiting reaction (*35*). Therefore, as expected, wide field-of-view TEM of 0.5 nm ZrO_2 (fig. S2A) illustrates the ultrathin ZrO_2 layer is continuous across a large area (~ 350 nm). Furthermore, as mentioned in the previous section, the X-ray beam footprint in the grazing incidence XRR and OOP diffraction experiments (tens of millimeters) provide additional thickness verification across a much wider area (Fig. S1) compared to the TEM imaging (hundreds of nanometers).

XRR X-ray reflectivity (XRR) fitting analysis (fig. S1B) was performed with the python package GenX (*43*), in which the underlying SiO_2 buffer layer and top ZrO_2 layer thicknesses were fitting parameters for ZrO_2 films ranging from 5 to 100 ALD cycles in thickness. The extracted growth rate from XRR is 0.97 Å ZrO_2 per ALD cycle (fig. S1B), which is close to the commonly reported ~ 1 Å/cycle growth rate for ALD-grown HfO_2- ZrO_2 (*11*). Furthermore, the growth rate is consistent with that extracted from out-of-plane (OOP) grain size analysis (fig. S1D).

Grain Size The out-of-plane (OOP) grain sizes (D) were determined via Scherrer's equation (*62*),

$$D = \frac{2\pi}{\Delta Q}$$

where $\Delta Q = \frac{4\pi \cos(\theta)\Delta(2\theta)}{2\lambda}$, θ corresponds to either the $(101)_t$ peak or the $(111)_o$ peak, and $\Delta(2\theta)$ is the full width at half maximum (FWHM). The above equation was applied to the OOP-GID spectra for the ZrO_2 thickness series (fig. S1C). For ZrO_2 films below 10 nm ($\leq$ 7 nm), the OOP grain size is constrained by the ZrO_2 physical thickness (fig. S1D); therefore, OOP grain size in the ultrathin limit serves as a gauge of the ZrO_2 thickness. The growth rate determined from this analysis (0.93 Å ZrO_2 per ALD cycle) is consistent with that determined from XRR (fig. S1B).

TEM The confirm the thickness of the 5 ALD cycle thick ZrO_2 layer, local cross-section HR-STEM images (fig. S2) were analyzed with DigitalMicrograph software using a line profile ~ 3 nm with integration width ~ 30 nm. Due to the angstrom-level roughness, the red boundary lines are determined by eye based on layer color contrast; the ultrathin ZrO_2 layer was surrounded by

high contrast neighboring layers (low-Z SiO_2 underlayer and low-Z Al_2O_3 capping layer) to aid in layer delineation. Slight roughness is expected due to the non-sharp interfaces present in non-epitaxial ALD-grown films on non-crystalline templates (e.g. amorphous SiO_2). Furthermore, beam damage from milling during TEM sample preparation could potentially introduce another source of roughness. On the other hand, no sample preparation is required for XRR and X-ray based measurements, just the uncapped ZrO_2 film is necessary. These contributions help explain why the thickness extracted from the local TEM imaging (fig. S2C, 0.58 nm) is slightly thicker than the thickness extracted from the grazing X-ray techniques (fig. S1, ~ 0.5 nm).

Structural Analysis

Oxygen imaging analysis Original atomic-resolution studies of HfO_2-ZrO_2-based ferroelectrics employed high-angle annular dark-field scanning transmission electron microscopy (HAADF STEM) to identify various fluorite-structural polymorphs (*48*). While this technique can successfully identify various fluorite-structure polymorphs in HfO_2-ZrO_2 thin films (*10, 49, 50*), it is not sensitive to subtle oxygen acentric displacements; HAADF STEM contrast preferentially highlights the more strongly scattering cation atoms relative to the more weakly scattering oxygen anions. Other works aimed to distinguish the different orthorhombic space groups based on mirror symmetry-breaking employed the position-averaged convergent beam electron diffraction (PACBED) method (*51*), which implies the existence of non-centrosymmetric orthorhombic *Pca*2_1 structure in doped-HfO_2 thin films (*49*); however, this technique still does not provide definitive evidence of the polar *Pca*2_1 phase.

To address this limitation, electron microscopy work shifted to oxygen-sensitive techniques to more directly identify the ferroelectric phases in this material system, which included integrated differential phase contrast (iDPC) STEM (*19,52*), aberration-corrected STEM-ABF (*53*) and negative spherical aberration imaging (NCSI) (*20*). In this work, we employ the NCSI technique for oxygen imaging analysis (*54, 55*), in which the oxygen atoms can become visible under certain experimental conditions. The HR-TEM image simulations (*37, 38*) were calculated close to the experimental imaging conditions (Materials and Methods, fig. S6) along various zone axes for the tetragonal *P*4_2*/nmc* structure and the orthorhombic *Pca*2_1 structure (fig. S5) to match with the experimental HR-TEM imaging of 5 nm ZrO_2 and 2 nm ZrO_2 (Fig. 1), respectively. In particular, the HR-TEM simulation of the orthorhombic *Pca*2_1 along the [110] zone axis under the experimental NCSI conditions clearly demonstrate alternating rows of zig-zag and blurred oxygen arrangements, which match well with the experimental data for 2 nm ZrO_2 films (Fig. 1G, fig. S6).

Cation imaging analysis Beyond oxygen imaging analysis, traditional cation imaging can also provide supplemental confirmation of the crystal structures indexed by NCSI. In particular, the cation-cation bond angle between neighboring Zr atoms demonstrate a very close match to HRTEM simulations (fig. S7) for both the tetragonal *P*4_2*/nmc* structure (5 nm ZrO_2 films) and the orthorhombic *Pca*2_1 structure (2 nm ZrO_2 films) along the [001] and [110] zone axes, respectively.

Ferroic phase identification via diffraction analysis For fluorite-structure thin films, the main structural polymorphs to consider are the dielectric monoclinic ($P2_1/c$), antiferroelectric tetragonal ($P4_2/nmc$), and ferroelectric orthorhombic ($Pca2_1$) phases. Various diffraction

reflections from the wide-angle GiD spectra enable indexing to the orthorhombic $Pca2_1$ and tetragonal $P4_2/nmc$ phases. Lattice parameters (a, b, c) – determined via Bragg's law from the d_{200} family of reflections – are self-consistently checked against the (111) ($\frac{1}{d_{111}^2} = \frac{1}{a^2} + \frac{1}{b^2} + \frac{1}{c^2}$) and (101) ($\frac{1}{d_{101}^2} = \frac{1}{a^2} + \frac{1}{c^2}$) lattice spacings, as well as other higher-order reflections, for the ferroelectric o-phase and antiferroelectric t-phase, respectively (fig. S4). The presence of monoclinic phase fraction is ruled out based on the lack of its characteristic split {111} reflections in the diffraction spectra, which would have been sufficiently separated from the $(111)_o$ and $(101)_t$ reflections. The tetragonal $(101)_t$ reflection is distinguished from the orthorhombic $(111)_o$ reflection in ultrathin (2 nm and below) films (Fig. S4D-F) based on the self-consistent indexing methodology detailed above. From the indexing analysis, we find the tetragonal $(101)_t$ reflection has a smaller d-spacing than the orthorhombic $(111)_o$ reflection, consistent with results in thicker HfO_2-ZrO_2-based films (*56,57*).

Structural distortion analysis: aspect ratio The aspect ratios (Fig. 2A) of the antiferroelectric t-phase (c/a) and the ferroelectric o-phase ($2c/(a + b)$) provide an indication of the degree of lattice distortion present in their respective structures, as recently investigated for ALD-grown ferroelectric Zr:HfO_2 films (*11*) and ALD-grown antiferroelectric ZrO_2 films (*58*). The aspect ratios were computed from the extracted lattice parameters based on the self-consistent indexing methodology detailed above. In particular, the aspect ratio of the o-phase exceeds that of the t-phase for fluorite-structure oxides (*56,59*). Notably, the lattice distortion present in ZrO_2 is enhanced in the ultrathin regime – opposite to the typical tetragonal distortion trend in perovskite ferroelectrics (*60*) – indicative of the "reverse" size effects present in fluorite-structure ferroelectrics. For example, the tetragonal aspect ratio was shown to decrease with decreasing thickness in ferroelectric $PbTiO_3$ films (*60*), while the orthorhombic aspect ratio is substantially enhanced in the ultrathin regime for fluorite-structure Zr:HfO_2 films (*11*).

Structural distortion analysis: interplanar lattice spacing Another structural marker, the interplanar lattice spacing (d_{101-T}, d_{111-O}), also indicates ultrathin-amplified distortions in the ZrO_2 films (Fig. 2A). The origin of the left-shift in the $(111)_o$ ($(101)_t$) reflection with decreasing thickness is typically attributed to the phase fraction distribution from the antiferroelectric t-phase towards the ferroelectric o-phase; the left-shift of the peak in reciprocal space corresponds to an increase in real-space lattice spacing. In particular, the ferroelectric o-phase d_{111}-spacing (>3.03 Å) for ZrO_2 in the ultrathin regime (< 2 nm) is larger than typical values for thick ferroelectric HZO films (2.95 Å) (*21*), demonstrating that ZrO_2 is in fact strained i.e. increased rhombic distortion. This is consistent with the ultrathin-enhanced lattice distortions trend observed in previous ALD-grown highly-oriented orthorhombic ferroelectric Zr:HfO_2 films (*11*) as well as PLD-grown epitaxial orthorhombic ferroelectric Zr:HfO_2 films (*26*). On the other hand, we observe that the t-phase d_{101} spacing (2.91-2.95 Å) in thicker ZrO_2 films (~4-10 nm) is nearly the same as is expected for prototypical antiferroelectric t-ZrO_2 (2.94 Å) (*21*). This is expected: when the tetragonal phase is strained with decreasing thickness, it transitions to the lower symmetry orthorhombic phase as opposed to remaining in the tetragonal phase, as it does not have the same tolerance of the FE o-phase to maintain its symmetry when strained. Consequently, the larger d-spacing is attributed to the FE o-phase (*56*), as confirmed by self-consistent indexing to higher-order reflections (fig. S4). These results, along with the findings reported in previous ALD-grown highly-oriented orthorhombic ferroelectric Zr:HfO_2 films (*11*),

ALD-grown polycrystalline antiferroelectric ZrO_2 films (*58,61*), as well as PLD-grown epitaxial orthorhombic ferroelectric Zr:HfO_2 films (*26*), indicate ultrathin-enhanced lattice distortions might be inherent to the symmetry present in fluorite-structure oxides, in stark contrast to the size effects typically present in the prototypical perovskite-structure oxide ferroelectrics (*6,7*).

Crystal field splitting X-ray spectroscopy provides various signatures to distinguish the competing ferroelectric o-phase and antiferroelectric t-phase in fluorite-structure thin films (*11,63*). Simulated XAS spectra for ZrO_2 in the various fluorite-structure polymorphs (orthorhombic *Pca*2_1 and tetragonal *P*4_2*/nmc*) were computed through the Materials Project (*64*) open-source database for XAS spectrum (*65*); previous work on ultrathin ferroelectric Zr:HfO_2 films (*11*) provides additional details on the symmetry-specific spectroscopic signatures. The t-phase ($P4_2$/nmc) nonpolar distortion (D_{4h}, 4-fold prismatic symmetry) from regular tetrahedral (T_d, full tetrahedral symmetry) fluorite-structure symmetry does not split the degenerate *e*-bands ($d_{x^2-y^2}$, $d_{3z^2-r^2}$), as confirmed by experiment (*63*) and the aforementioned XAS simulations. Meanwhile, the o-phase ($Pca2_1$) polar rhombic pyramidal distortion (C_{2v}, 2-fold pyramidal symmetry) does split the *e* manifold based on crystal field symmetry, providing a spectroscopic means to distinguish the tand o-phases i.e. the additional spectroscopic feature present between the main *e*- and t_2- absorption features due to this additional symmetry-lowering distortion. The O *K*-edge XAS spectra demonstrates tetrahedral and rhombic splitting features closely matching the polar o-phase ($Pca2_1$) emerging for ZrO_2 in the sub-2 nm range, indicative of the ultrathin-enhanced emergence of the ferroelectric o-phase. This demonstrates a spectroscopic fingerprint for phase identification beyond diffraction which can often be ambiguous due to the nearly identical t- and o-phase lattice parameters (*56*). The symmetry-specific crystal field distortions in ZrO_2 films also evolve with thickness; the tetrahedral (rhombic) crystal field Δ_T (Δ_R) arising from the T_d (C_{2v}) symmetry in ultrathin ZrO_2 films sharply increases below 3 nm thickness (Fig. 2B), suggesting the increased emergence of ferroelectric o-ZrO_2 in ultrathin films, consistent with thickness-dependent diffraction trends (Fig. 2A)

Orbital polarization In conjunction with XAS, x-ray linear dichroism (XLD) can also probe structural distortions due to its sensitivity to orbital asymmetry, which can arise from inversion symmetry breaking. For example, in perovskite ferroelectrics $PbTiO_3$ and $BaTiO_3$, the Ti 3*d* - O 2*p* orbital hybridization is essential for stabilizing the noncentrosymmetric ferroelectric structure (*66*). Particularly at the 3*d* cation $L_{3,2}$ edge, orbital polarization extracted from XLD is used as a measure of the oxygen octahedral distortion in perovskites due to the anisotropic hybridization between cation 3*d* and O 2*p* orbitals (*67*). Accordingly, in fluorite-structure ferroelectrics, the magnitude of XLD present at the Zr $M_{3,2}$ and Zr $L_{3,2}$ edges can be a gauge of the degree of polyhedral distortion – in this case distortion of oxygen tetrahedron – and the oxygen atomic asymmetry (*11*). Indeed, the orbital polarization at these Zr edges is enhanced as the thickness is reduced from the thick (10 nm) to ultrathin (5 Å) regime (fig. S8D), consistent with diffraction results also demonstrating amplified structural distortions in the ultrathin limit.

Optical Analysis

Polarization insights from SHG Nonlinear optical microscopy also supports the size-dependent ferroic phase evolution, as the observed increase in second harmonic generation (SHG) signal with decreasing ZrO_2 thickness (Fig. 2C, fig. S11) is consistent with the structural

trends indicating the ultrathin-enhanced FE polarization (Fig. 2A,B). Indeed, SHG intensity has been shown to directly map to the polarization across the composition space in 20 nm thick HfO_2-ZrO_2 solid solutions (*68*). The exception to the ultrathin-enhanced polarization trend from SHG spatial mapping measurements (Fig. 2C) occurs for 5 Å ZrO_2, which can be potentially attributed to an amorphous phase fraction expected in such ultrathin films deposited at low temperature (300°C). The SHG spot size can engulf both crystalline regions in the polar o-phase and amorphous regions, so the averaged SHG signal can be weighed down by this amorphous fraction; meanwhile, the other structural signatures (Fig. 2A,B) are only sensitive to the crystalline regions.

SHG sensitivity to in-plane polarization In the SHG measurement configuration (fig. S12), a linearly polarized femtosecond laser beam impinges on the sample surface in the normal direction, which results in in-plane polarization electric field. According to the assigned physical coordinate with respect to the lab coordinate for in-plane polarized regions of sample, the electric field of fundamental light has components $\boldsymbol{E}^{\omega}(\theta) = (-E_0 sin\theta, 0, E_0 cos\theta)$. Here, θ is the azimuthal angle of the fundamental light polarization, and the ω subscript denotes the frequency of the fundamental light.

The light-induced nonlinear polarization in the in-plane polarized regions of the $Pca2_1$ structure (*2mm* point group) can be obtained as follows:

$$\begin{pmatrix} P_x \\ P_y \\ P_z \end{pmatrix} = \begin{bmatrix} 0 & 0 & 0 & 0 & d_{15} & 0 \\ 0 & 0 & 0 & d_{15} & 0 & 0 \\ d_{15} & d_{15} & d_{33} & 0 & 0 & 0 \end{bmatrix} \begin{pmatrix} E_x^2 \\ E_y^2 \\ E_z^2 \\ 2E_yE_z \\ 2E_xE_z \\ 2E_xE_y \end{pmatrix} = E_0^2 \begin{pmatrix} -2d_{15}\sin\theta\cos\theta \\ 0 \\ d_{31}\sin^2\theta + d_{33}\cos^2\theta \end{pmatrix}.$$

And our experimental configuration collects in-plane electric field components of SHG light as follows:

$$I_x^{2\omega} \propto |\boldsymbol{P}\cdot\boldsymbol{A_x}|^2 \propto |d_{31}\,sin^2\theta + d_{33}\,cos^2\theta|^2$$
$$I_y^{2\omega} \propto \left|\boldsymbol{P}\cdot\boldsymbol{A_y}\right|^2 \propto |2d_{15}\,sin\,\theta\,cos\,\theta|^2$$

where $\boldsymbol{A_i}$ corresponds to the orientation of the output analyzer in position *i* (expressed, $\boldsymbol{A_x} = (0,0,1)$ and $\boldsymbol{A_y} = (0,0,1)$. The SHG experimental setup does not use a polarizer; therefore, the total SHG emission measured by its configuration is $I_x^{2\omega}$+$I_y^{2\omega}$. The non-zero d_{ij} components indicate that in-plane polarized regions of this thin film can produce non-zero SHG light captured by this measurement configuration.

Meanwhile, for out-of-plane polarization, the electric field of fundamental light has components $\boldsymbol{E}^{\omega}(\theta) = (E_0 cos\theta, -E_0 sin\theta, 0)$. Then, the nonlinear polarization is

$$\boldsymbol{P} = E_0^2 \begin{pmatrix} 0 \\ 0 \\ d_{31}\cos^2\theta + d_{32}\sin^2\theta \end{pmatrix}.$$

Applying $\boldsymbol{A_x} = (1,0,0)$ and $\boldsymbol{A_y} = (0,1,0)$, both $I_x^{2\omega}$ and $I_y^{2\omega}$ become zero.

Thus, this result indicates that our SHG measurement configuration is exclusively sensitive to in-plane polarizability of the $Pca2_1$ structure (*2mm* point group). Indeed, an in-plane projection of the polarization is expected in the ultrathin ferroelectric ZrO2 films based on its predominant orientation (fig. S3, Main Text).

Regarding the nonpolar $P4_2/nmc$ tetragonal phase (*4/m* point group) present in thicker ZrO_2 films, the piezoelectric matrix is empty; therefore, no light-induced nonlinear polarization is expected for these nonpolar structures.

Electrical Analysis

Dielectric permittivity extraction from MOS capacitors The permittivity of ZrO_2 was extracted from thickness-dependence MOS *C-V* measurements (fig. S9) on lightly-doped p-type substrates. In the accumulation region of the MOS *C-V* measurements, the MOS capacitor can be modelled as three capacitors (ZrO_2 layer, SiO_2 layer, and Si space charge layer) in series using the following equation,

$$\frac{1}{C} = \frac{1}{\epsilon_0 \epsilon_{ZrO_2}} t_{ZrO2} + \frac{1}{\epsilon_0 \epsilon_{SiO_2}} \left[t_{SiO_2}^{phys} + \frac{t_{CL} \epsilon_{SiO2}}{\epsilon_{Si}} \right]$$

where t_{ZrO_2} is the thickness of the ZrO_2 layer, t_{SiO2}^{phys}, is the physical SiO_2 thickness, and t_{CL} is the charge layer thickness in silicon. The physical SiO_2 thickness is constant across all ZrO_2 film thicknesses. Additionally, the capacitance values were extracted at a fixed charge of Q = -1 μC/cm^2 which ensures that the charge-layer thickness is constant across all thicknesses and in the accumulation region. Therefore, from Equation 3, the inverse capacitance at a fixed charge as a function of ZrO_2 thickness should result in a line and the permittivity of the ZrO_2 layer can be extracted from the slope.

Polarization switching via tunnel junctions *I-V* measurements in tunnel junctions overcome shortcomings faced by conventional ferroelectric *P-V* and *C-V*, piezoresponse, and synchrotron X-ray techniques by leveraging tunnel currents, disentangling competing hysteretic mechanisms, and demonstrating polarization switching, respectively. For example, hysteresis loops from polarization-voltage (*P-V*) and capacitance-voltage (*C-V*) measurements – the traditionally-demonstrated smoking-gun evidence of polarization switching – become obsolete in the ultrathin regime once leakage currents dominate switching current and distort the extracted behavior (*69*). Meanwhile, tunnel junctions exploit the tunnel current via its polarization-dependence, allowing for ferroelectric measurements in the sub-5 nm regime. Tunnel junctions *I-V* measurements also overcome the key limitation of synchrotron X-ray characterization, which can bypass leakage to examine polar symmetry in ultrathin films, but fail to demonstrate polarization switching (*70,71*). Piezoresponse measurements can also eliminate leakage and demonstrate polarization switching, but its electrically-modulated tip deflection can be confounded by various electrochemical, electromechanical, and electrostatic artefacts which can give rise to hysteretic piezoresponse (*42,72*). Therefore, characterizing ultrathin ferroics via tunnel junctions (Fig. 3C, fig. S14) present a complementary *I-V* methodology for disentangling confounding hysteretic mechanisms from polarization switching, serving as a promising metrology tool for advanced nanoelectronics (*73*) in tandem with scanning probe microscopy (*74*). Indeed, *I-V* measurements have been previously employed to demonstrate ultrafast polarization switching in thicker ALD-grown HfO_2-ZrO_2 thin films (*75–79*). Furthermore, in other ferroelectric material systems, FTJ *I-V* measurements have been used to pinpoint ferroelectric origins in both ultrathin oxides (*80, 81*) and emerging two-dimensional systems exhibiting hysteretic resistive switching (*82*).

Distinguishing polarization switching via electrical measurements It is worth noting that oxygen-vacancy-based contributions can be intertwined with polarization switching in oxide

ferroelectrics; indeed, some degree of influence of electrochemical phenomena intertwined with ferroelectric polarization switching has been observed for both perovskite-based (*83–88*) and fluorite-based (*19, 89–93*) FTJs. In particular, voltage-driven oxygen vacancy migration is the commonly employed resistive switching mechanism in resistive random access memories (RRAMs) (*94,95*), in which oxygen vacancies form conductive-filaments within the dielectric barrier layer. Therefore, to examine potentially confounding ionic and electrochemical contributions in the ultrathin ZrO_2 FTJs, further *I-V* measurements were performed.

In particular, voltage polarity-dependent pulsed *I-*V_{write} hysteresis measurements (fig. S14D) are able to rule out filamentary-type resistive switching mediated by electrochemical ionic-driven mechanisms. For typical bipolar filamentary-mediated resistive switching, the filament formation set by the first polarity results in the high-current state; therefore, the sense of hysteresis is dependent on the direction of the voltage sweep (*96*). Meanwhile, for polarization-mediated switching, the polarization-induced band modulation sets the current states; the polarization direction in the ferroelectric barrier is set by the polarity of the voltage pulse, independent of the sweep direction. Therefore, for polarization-driven switching, the same *I-*V_{write} hysteresis sense should be observed independent of the sweep direction, consistent with the behavior observed in the ultrathin ZrO_2 FTJs (fig. S14D). Additionally, the measured pulsed-*I-V* hysteresis loops for ultrathin ZrO_2 (Fig. 3C, fig. S14D), which shows two stable resistance states – corresponding to the two remnant polarization states – match piezoresponse hysteresis loops (fig. S14C), also strongly suggestive of polarization-driven switching (*97*). Furthermore, the observed counter-clockwise hysteresis sense (Fig. 3C, fig. S14D) is consistent with polarization-induced barrier height modulation as depicted in the electron band diagrams (fig. S14E) – positive voltage applied to the top electrode results in a lower average barrier height, and therefore, operates as the high current state. Moreover, the presence of closed hysteresis loops likely preclude ionic-driven mechanisms, which have been shown to result in open resistive hysteresis loops in HfO_2-based junctions (*89, 92*), likely due to irreversible oxygen vacancy migration. The lack of a forming step at high voltage required to observe resistive hysteretic switching also renders ionic-driven filamentary-based mechanisms unlikely.

All of the aforementioned behaviors to eliminate effects related to charge injection and demonstrate polarization-driven resistive switching have been established in previous works on similar ultrathin FTJs integrating ALD-grown 1 nm Zr:HfO_2 barriers on SiO_2-buffered Si (*11,23*). Therefore, although the co-existing, and often synergistic (*19,89*) influence of various electrochemical and ionic phenomena intertwined with polarization switching cannot be completely eliminated, multiple *I-V* signatures in these ultrathin ZrO_2 FTJs indicate minimal contributions from various ionic-driven mechanisms and indicate the observed resistive switching behavior is consistent with ferroelectric polarization switching.

Such charge injection concerns are even less likely for the in-plane IDE *P-V* measurements (Fig. 3, fig. S10,15) considering IDE structures ($\sim 1\ \mu$m oxide barrier) possess significantly lower leakage current compared to that present in out-of-plane tunnel junctions ($\sim$ 1 nm oxide barrier).

Distinguishing polarization switching via scanning probe microscopy Regarding scanning probe microscopy (SPM) images (fig. S13), measures were taken to eliminate non-polarization-driven mechanisms of PFM contrast. AFM topography images before and after voltage poling ultrathin (0.5 nm, 1 nm) ZrO_2 films demonstrate no surface morphology changes to the films due to poling (fig. S13A,B), which indicate the strong PFM amplitude and phase contrast in ultrathin

ZrO_2 present after poling (fig. S13 C,D) are not artifacts from charge injection or other electrochemical origins. This also rules the possibility of cross-talk between topography and phase retraces leading to false phase contrast. Furthermore, PFM phase contrast for ultrathin (0.5 nm, 1 nm) ZrO_2 films persists after 2 hours; such long-term retention significantly suppresses shorter-scale effects such as charge injection, further suggesting that the PFM contrast is due to ferroelectric polarization behavior. Furthermore, the presence of spontaneous as-grown polarization further indicates that the observed PFM contrast upon voltage application is inherent to the film's polar nature, and not an extrinsic tip-induced artifact.

Origin of as-grown spontaneous polarization Notably, unpoled regions of ultrathin (0.5, 1 nm) ZrO_2 films demonstrate the same PFM phase contrast as positively poled regions (fig. S13D), indicating that ultrathin ZrO_2 exhibits spontaneous polarization. Regarding the origin of this spontaneous polarization, the spectroscopic signatures of ultrathin-enhanced polar distortion (Fig. 2) indicate the presence of a polarization and the highly-oriented nature of the ultrathin films (fig. S3) requires the presence of an out-of-plane (OOP) projection of the $Pca2_1$ polar axis; therefore, this OOP polarization would be detected by the PFM measurement. These reasons establish why a spontaneous OOP polarization is expected to be present. To explain why one polarization state over the other is preferred, the nature of the SiO_2/ZrO_2 interface must be considered. The high-κ oxide and semiconductor device community has extensively characterized interface traps states (D_{it}) at SiO_2-HfO_2 and SiO_2-ZrO_2 interfaces, inherent to low-temperature ALD deposition on amorphous (SiO_2) templates; these states can serve as bound charges at the interface, which would in turn, prefer a specific (up or down) polarization state. The preferred polarization in ultrathin (0.5, 1 nm) ZrO_2 films points toward silicon, consistent with negatively charged bound charges at the SiO_2-ZrO_2 interface.

Fluorite-Structure Ferroelectric Considerations

ZrO_2 versus HfO_2 To help unravel these curious size effects, key fluorite-structure insights can be derived from the competing symmetries inherent to its rich polymorphic nature (*15*), particularly surface energy (*98*) contributions. Thermodynamic (*99*,*100*) and kinetic (*99*) contributions help explain why ZrO_2 is preferred to its sister fluorite-structure binary oxide HfO_2 for stabilizing the ferroelectric o-phase in the ultrathin regime. In particular, the low temperature of crystallization for ZrO_2 relative to HfO_2 (*101*) eliminates potential reversion back to the bulk-stable paraelectric monoclinic formation, which has been observed upon cooling after the typical high-temperature post-deposition annealing usually required for phase crystallization in HfO_2-based thin films (*102*). Crystallizing ZrO_2 at low temperatures during the ALD deposition itself avoids such kinetic effects (*99*), which allows dimensionality-driven size effects (discussed in Main Text) to maintain as the major energy driving force, thereby keeping the metastable ferroelectric o-phase trapped.

Fluorite-structure antiferroelectricity We note here that the original Kittel view of an "antipolar" crystal structure with two sublattices of opposite polarization (*103*) does not seem to apply to the nonpolar $P4_2/nmc$ tetragonal lattice attributed to fluorite-structure antiferroelectricity (*104*). Instead, the more inclusive definition of antiferroelectricity put forth in recent years (*105*) – i.e. reversible field-dependent first-order nonpolar-to-polar phase transition without explicitly requiring an anti-polar phase – more accurately describes this fluorite-structure system. The

expected field-induced nonpolar-to-polar (tetragonal $P4_2/nmc$ to orthorhombic $Pca2_1$) phase transition for fluorite-structure antiferroelectrics (*104*) was first theoretically established (*24*) and later experimentally demonstrated via field-dependent diffraction (*106*), electron microscopy (*107,108*), scanning probe microscopy (*61*) and electrical measurements (*109*) in Hf:ZrO_2 and ZrO_2 thin films. In this work, the relatively thick ZrO_2 films indeed index to the nonpolar tetragonal $P4_2/nmc$ (Fig. 1, S4, S5, S8) and exhibit the characteristic antiferroelectric-like double-hysteresis behavior (Fig. 3B, E); therefore, our results are consistent with the more recent picture of antiferroelectricity (*105*) – i.e. field-induced ferroelectric state – that has been ascribed to the HfO_2-ZrO_2 family (*104*).

The distinguishing feature of this work is we instead focus on the thickness-driven – rather than field-driven – nonpolar t-phase to polar o-phase transition driven by reduced dimensionality in ZrO_2 thin films. Original studies into fluorite-structure systems examined the ferroelectric-antiferroelectric phase competition as a function of temperature and composition in thick (> 10 nm) films (*4,110–112*). More recent studies have examined antiferroelectricity down to the 4-5 nm regime in ALD-grown Hf:ZrO_2 (*76*) and ZrO_2 (*58,61,113,114*), but to date, the ultrathin (< 2 nm) regime has yet to be examined for fluorite-structure antiferroelectrics. Therefore, the size-driven antiferroelectric-to-ferroelectric phase transition has yet to be observed due to the unconventional size effects intrinsic to fluorite-structure ferroelectrics (discussed in Main Text), e.g. the sensitivity of t-phase and o-phase relative free energies to reduced size and surface energy effects (*21,115*).

<u>Depolarization field considerations</u> Besides the unique piezoelectric origins, unconventional ferroelectric origins have also been attributed to the fluorite-structure binary oxides (*12,13*). First-principles calculations suggest improper origins (*12*) may facilitate the persistence of atomic-scale ferroelectricity, as 2D fluorite-structure $Pca2_1$ layers have minimal depolarizing field associated with its structure, enabling unsuppressed polarization down to the u.c. thickness limit (*12,13*). Depolarization fields are the electrostatic penalty for electric dipoles at the ultrathin scale; accordingly, ferroelectricity in conventional perovskite oxides is typically suppressed at the few nanometer scale (*29*), as metals with finite screening cannot completely compensate the surface dipole charges (*2*). The ultrathin o-ZrO_2 films in this work are able to overcome depolarization effects, which would otherwise prohibit sustained polarization in the atomic-scale regime, due to its in-plane polarization, as evidenced by SHG mapping (Fig. 2C) and in-plane polarization switching (Fig. 3). For these films, the dominant out-of-plane orientation is the (111) (fig. S3); this close-packed plane is expected to be favored in the ultrathin regime due to the enhanced importance of surface energies at reduced dimensions. Considering the polar axis for the $Pca2_1$ structure is along a principal lattice direction, o-ZrO_2 films demonstrate a significant in-plane polarization component. Therefore, the highly-oriented nature of the ultrathin ZrO_2 films also contribute to the sustained atomic-scale electric polarization. In fact, van der Waals (vdW) chalcogenides have recently emerged to overcome ultrathin ferroelectric limitations via in-plane polarization (*116*); for perovskite-based ferroelectrics, exploiting epitaxial strain to stabilize in-plane polarization (*117*) could similarly help bypass these depolarization concerns in the ultrathin regime. Furthermore, the improper origin of fluorite-structure ferroelectricity (*12,13*) helps make it secondary polar distortion impervious to depolarization effects (*28*).

System	Material	Thickness (Å)	Dipole	Polarization switching?	Ref.
vdW	h-BN	6.6	OOP	BL: *I-V* loop, PFM loop	(*118*,*119*)
vdW	Graphene	6.7	OOP	BL: *I-V* loop	(*120*)
vdW	SnTe	6*(12)	IP	*ML: no (BL: *I-V* loop)	(*121*)
vdW	SnS	6	IP	ML: *I-V* loop	(*122*)
vdW	$MoTe_2$	8	OOP	ML: PFM loop, no *I-V*	(*82*)
vdW	WTe_2	14	OOP	BL: *I-V* loop	(*123*)
vdW	In_2Se_3	12	OOP/IP	ML: PFM loop	(*124*)
vdW	BA_2PbCl_4	17*	IP	*No switching loops	(*125*)
vdW	$CuInP_2S_6$	40	OOP	PFM loop	(*126*)
Polymer	P(VDF-TrFE)	10	OOP	BL: *I-V* loop (Pyro)	(*127*)
Perovskite	$BaTiO_3$	10*	OOP	*2-3 uc: No switching loop	(*81*)
Perovskite	$PbTiO_3$	12*	OOP	*3 uc: No switching loop	(*70*)
Perovskite	$BiFeO_3$	4*(8)	OOP	*1 uc: No (2 uc: PFM loop)	(*80*)
Perovskite	$BiFeO_3$	8	OOP	2 uc: PFM loop, no *I-V*	(*128*)
Perovskite	$Pb(Zr,Ti)O_3$	6*	OOP	*1.5 uc: No	(*129*)
Fluorite	Zr:HfO_2	25	OOP	PFM loops	(*130*)
Fluorite	Zr:HfO_2	< 20	OOP	PFM loops	(*131*)
Fluorite	Zr:HfO_2	15	OOP	*P-V* loops	(*132*)
Fluorite	Zr:HfO_2	15*(50)	OOP	*No switching (*P-V* loops)	(*10*)
Fluorite	Zr:HfO_2	10	OOP	*C-V* & *I-V* loops	(*11*,*23*)
Fluorite	ZrO_2	5-6	OOP/IP	*P-V* & *I-V* loops	this work

Table S1. Atomic-scale demonstrations of ferroelectricity. Note some works prove inversion symmetry-breaking, but do not demonstrate hysteretic polarization switching (indicated by "*" symbols). Abbreviations: van der Waals (vdW); out-of plane (OOP); in-plane (IP); current-voltage (*I-V*); capacitance-voltage (*C-V*); polarization-voltage (*P-V*); unit cell (uc); monolayer (ML); bilayer (BL).

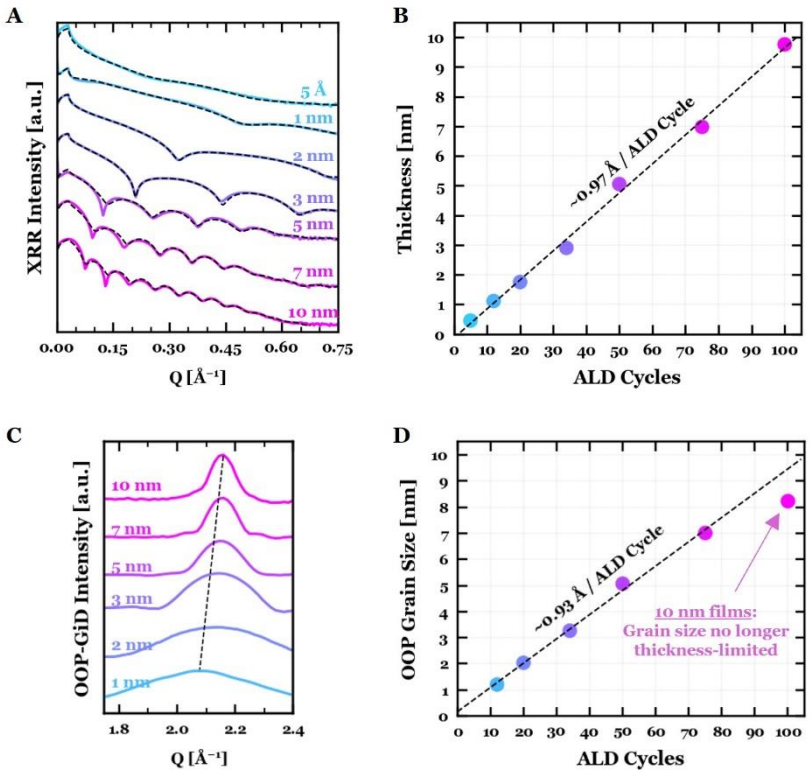

Fig. S1. Thickness verification of ALD-grown ZrO_2 via X-ray analysis. (**A**) Synchrotron X-ray reflectivity (XRR) of the ZrO_2 thickness series from 10 nm down to 0.5 nm thickness. The dotted black lines overlayed on the data are XRR simulations from which the thickness values reported in panel (B) are determined. (**B**) The extracted growth rate (~ 10 ALD cycles ≡ 1 nm thickness) is consistent with Zr:HfO_2 films extensively characterized in previous work on ultrathin Zr:HfO_2 films (*11*). (**C**) Out-of-plane grazing incidence diffraction (OOP-GiD) of the ZrO_2 thickness series. (**D**) Extracted growth rate from the OOP-GiD grain size analysis (Supplementary Text). Note for 10 nm (100 ALD cycles) films, the grain size is no longer limited by the thickness of the film, so this data point is not used for the thickness analysis.

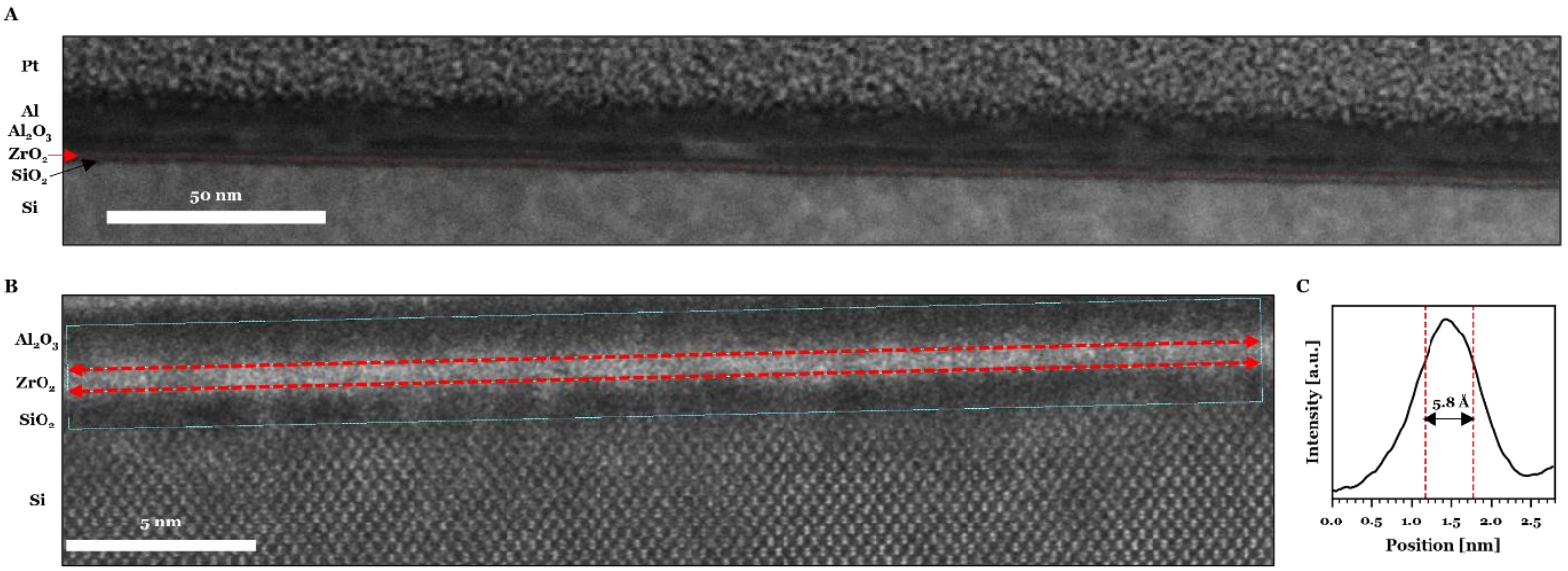

Fig. S2. Thickness verification of ALD-grown ZrO_2 via TEM analysis. (**A**) Wide field-of-view (FoV) HAADF-STEM image for a 5 ALD cycle ZrO_2 thin film on SiO_2-buffered silicon substrate illustrating the wide-area stability of ultrathin ZrO_2 layer (lighter contrast layer delineated by the faint red dotted lines) across ~ 350 nm FoV. **(B)** Zoomed-in HAADF-STEM image of the ultrathin ZrO_2 film from (A). **(C)** The ZrO_2 layer thickness is determined by line profile analysis. The ZrO_2 film (light contrast) examined here is capped with Al_2O_3 (dark contrast) to provide maximize Z-contrast in the dark field imaging mode to aid in layer delineation. The red boundary lines are determined by eye based on the color contrast. The blurred interfaces inherent to non-epitaxial ALD-grown films on amorphous underlayers (SiO_2) and capped with amorphous top layers (Al_2O_3) complicates TEM-based thickness extraction; therefore, X-ray based methodologies (fig. S1) are preferred for ultrathin thickness determination (Supplementary Text). Nonetheless. the extracted thickness of ~ 0.58 nm is close to the ~ 0.5 nm thickness determined from X-ray based techniques (fig. S1) for 5 ALD cycle ZrO_2 films.

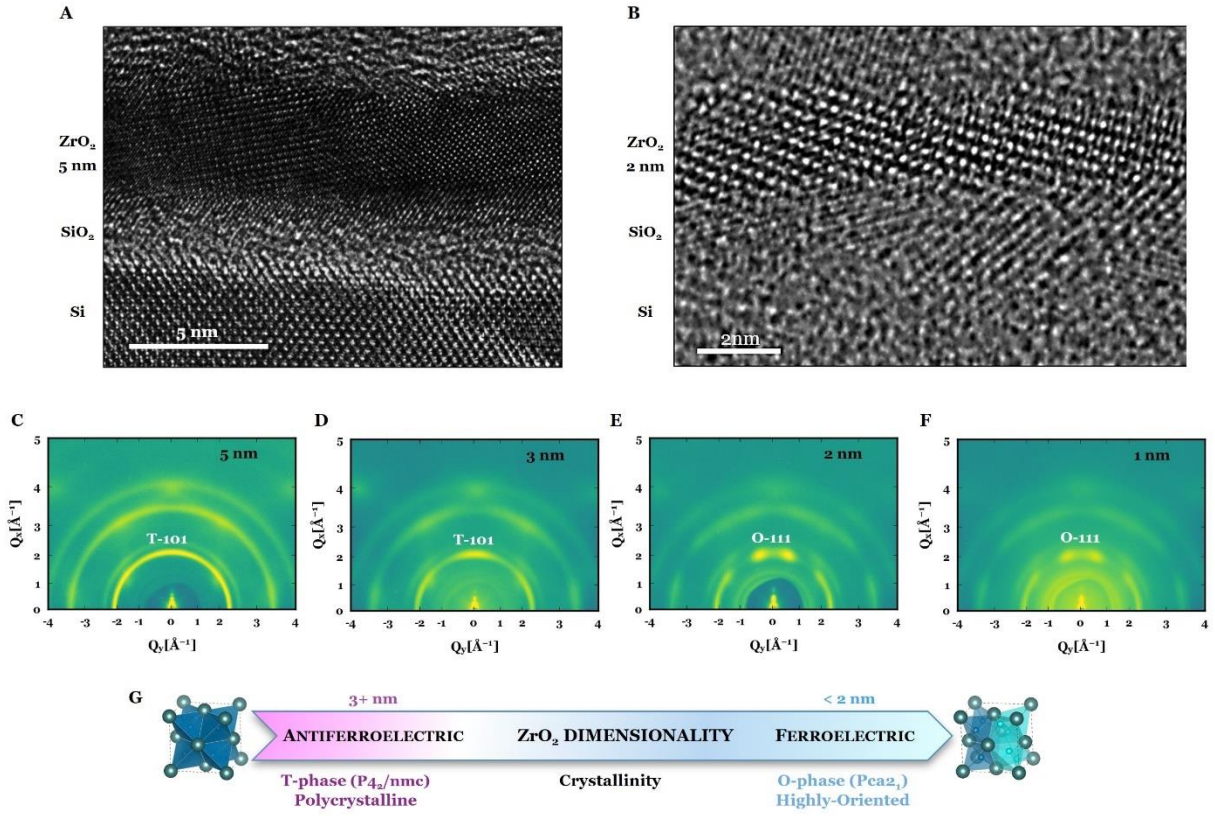

Fig. S3. Crystalline ultrathin ZrO_2 films. **(A,B)** Wide field-of-view cross-sectional TEM images of 5 nm (A) and 2 nm (B) ZrO_2 on SiO_2-buffered Si, used for the phase identification analysis (Fig. 1D-G) based on HR-TEM simulations (fig. S5). Note the Si substrate is tilted off its zone axis to image the crystallinity present more clearly in the 2 nm ZrO_2 layer. (**C,D,E,F**) 2D RSMs for 5 nm (C), 3 nm (D), 2 nm (E), and 1 nm (F) ZrO_2 on SiO_2-buffered Si, demonstrating the presence of crystalline films. Furthermore, the 2D maps indicate the emergence of enhanced texturing in ultrathin films ($\leq$ 3 nm) – consistent with previous work on ALD-grown ultrathin Zr:HfO_2 films (*11*, *131*) – illustrated by concentrated intensity spots rather than polycrystalline rings. The integrated 1D spectra also are consistent with the $P4_2/nmc$ and $Pca2_1$ indexing in thick and ultrathin films, respectively; in particular, the splitting of the reflection around $Q_x \sim 2$ Å^{-1} for films $\leq$ 2 nm suggests a symmetry-lowering transition from the $P4_2/nmc$ *T*-phase, consistent with the $Pca2_1$ *O*-phase. However, we note that the IP-GiD spectra (fig. S4) are used for more rigorous indexing analysis to the respective phases (Materials and Methods). These qualitative 2D diffraction maps are primarily meant to highlight the highly-oriented crystalline nature of the ultrathin ZrO_2 films. (**G**) Dimensionality-driven evolution of ZrO_2 from the antiferroelectric tetragonal phase to the ferroelectric orthorhombic phase illustrated through qualitative crystallinity features.

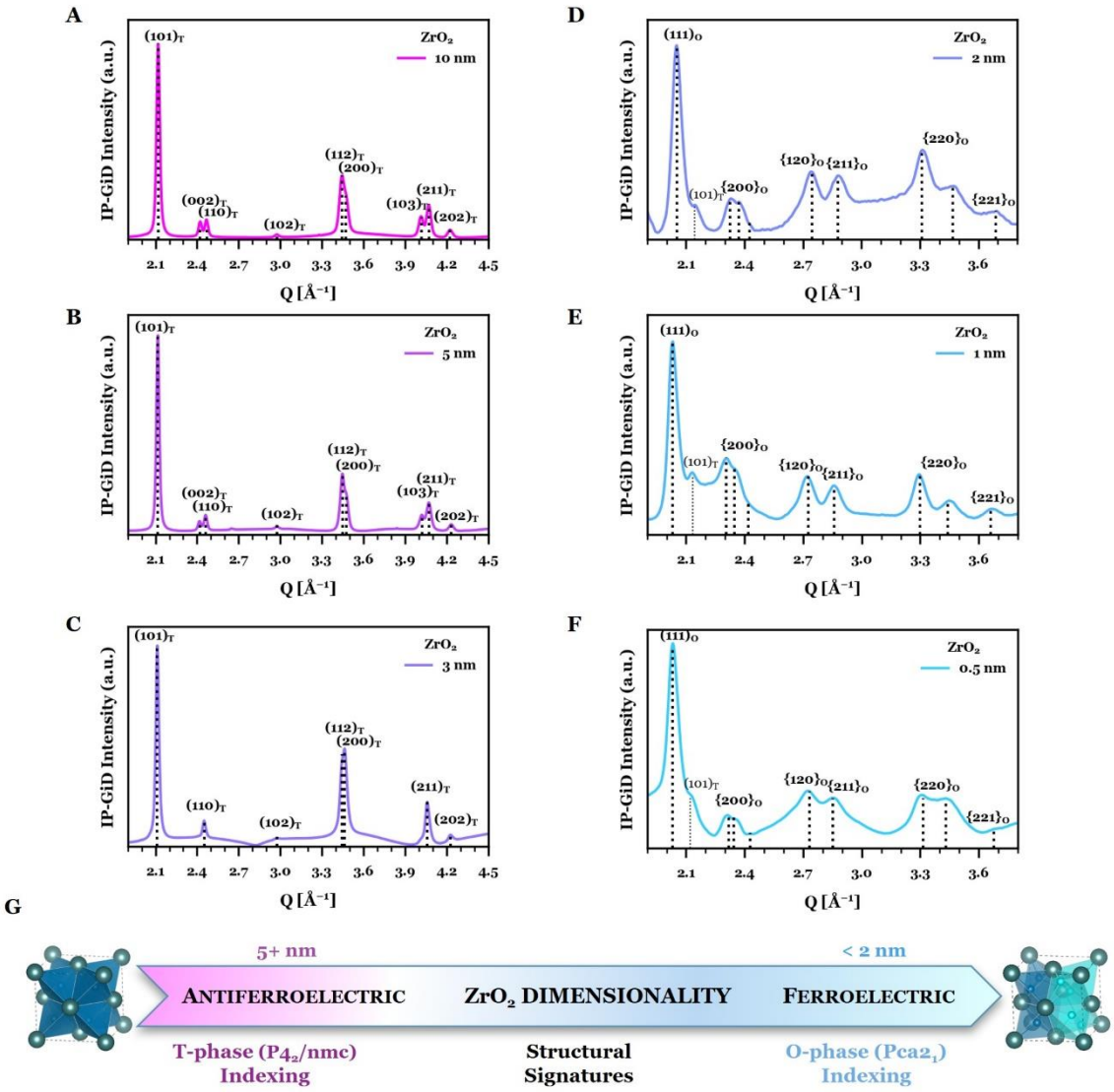

Fig. S4. Ferroic phase identification from synchrotron X-ray diffraction. (**A,B,C,D,E,F**) Synchrotron in-plane grazing incidence diffraction (IP-GiD) for the ZrO_2 thickness series in the relatively thick (10 nm, 5 nm, 3 nm) and ultrathin (2 nm, 1 nm, 5 Å) regime. In-plane GID indicates the presence of the antiferroelectric t-phase in relatively thick (> 2 nm) ZrO_2 films, while in-plane GID indicates an emergence of the ferroelectric o-phase for ZrO_2 films below 2 nm. 2 nm ZrO_2 marks the critical thickness for the symmetry-lowering tetragonal-to-orthorhombic structural phase transition, as illustrated by the increased number of reflections in ultrathin films, some of which are forbidden in the higher-symmetry t-phase. The detailed self-consistent indexing analysis considering multiple reflections is described in the Supplementary Text. (**G**) Dimensionality-driven evolution of ZrO_2 from the antiferroelectric tetragonal phase to the ferroelectric orthorhombic phase demonstrated through structural signatures from diffraction.

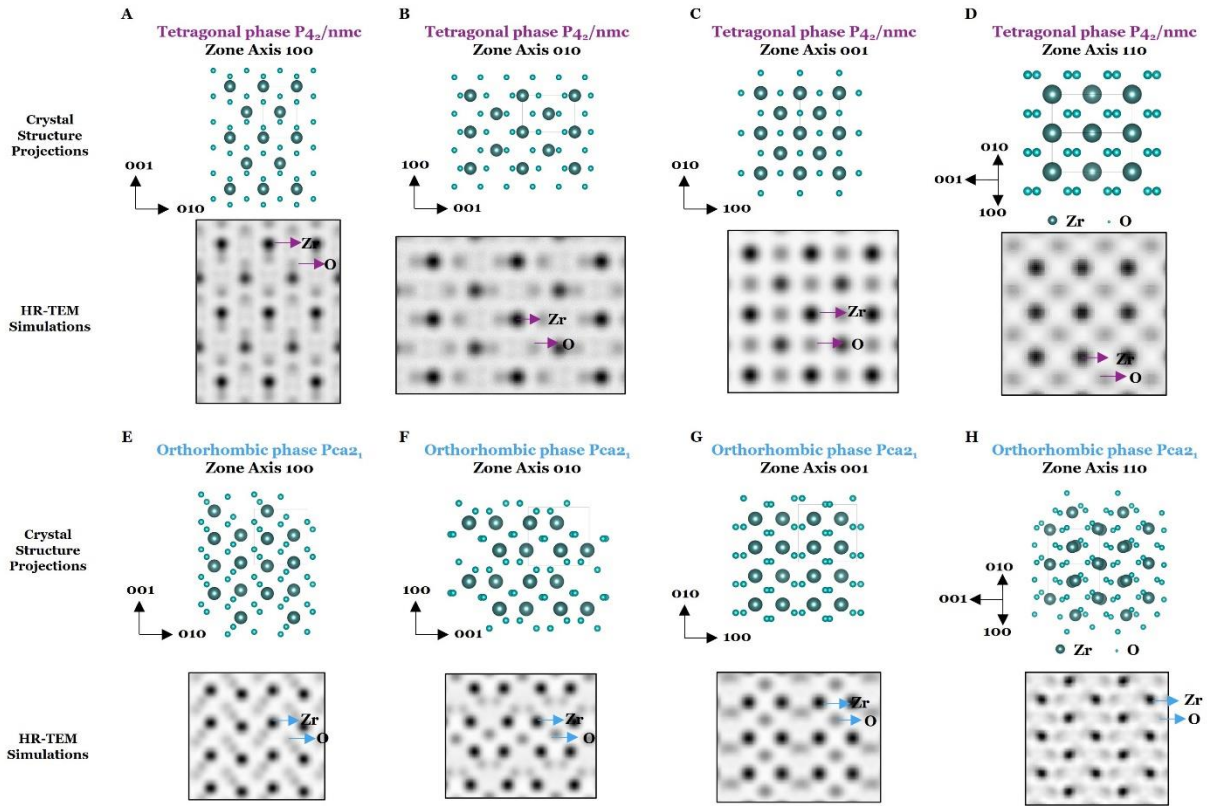

Fig. S5. Ferroic phase identification from oxygen imaging analysis. (**A,B,C,D**) Crystal structure projections (top) and HR-TEM simulations (bottom) along the 100 (A), 010 (B), 001 (C), and 110 (D) zone axes for the tetragonal *P*4$_2$*/nmc* structure. The experimental HR-TEM imaging of 5 nm ZrO_2 (Fig. 1D,E) matches with the [001] projection of crystal structure and TEM simulation for the tetragonal *P*4$_2$*/nmc* structure. (**E,F,G,H**) Crystal structure projections (top) and HR-TEM simulations (bottom) along the 100 (E), 010 (F), 001 (G), and 110 (H) zone axes for the orthorhombic *Pca*2$_1$ structure. The experimental HR-TEM imaging of 2 nm ZrO_2 (Fig. 1F,G) matches with the [110] projection of crystal structure and TEM simulation for the orthorhombic *Pca*2$_1$ structure. Note all HR-TEM simulations are provided in inverted contrast to better accentuate the oxygen atoms under the following conditions: specimen thickness ~ 10 nm and defocus = 4 nm (Materials and Methods).

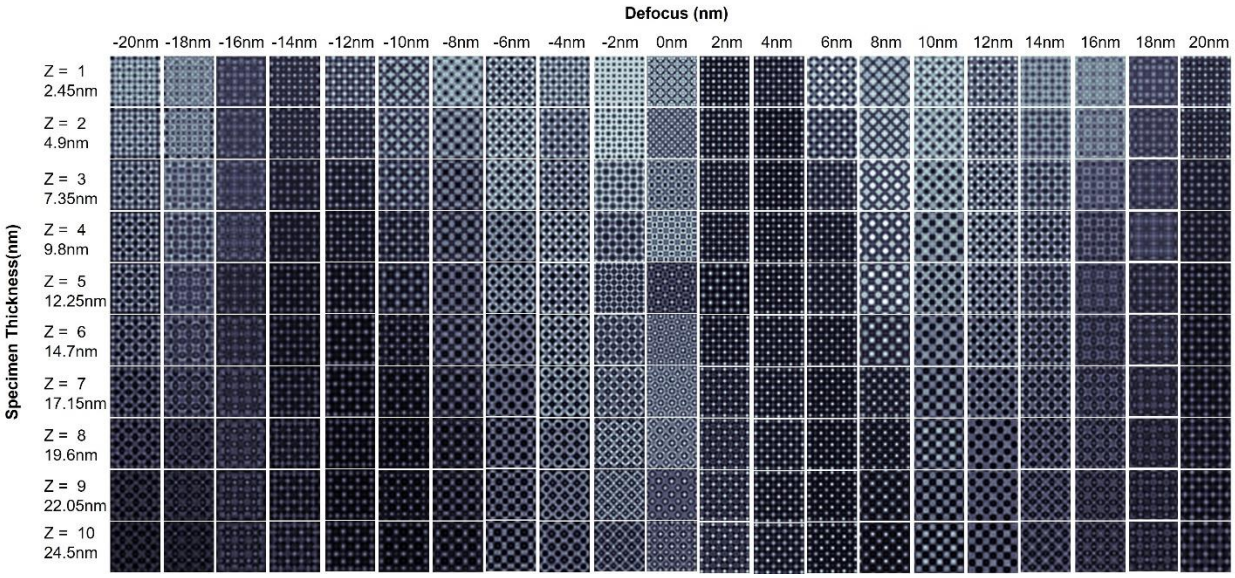

Fig. S6. Determining oxygen imaging conditions from HR-TEM simulations. Tetragonal $P4_2/nmc$ ZrO_2 HR-TEM simulations as a function of defocus value and TEM specimen thickness under the following experimental conditions: C_s = -16 μm, C_5 = 6.8 mm, slice thickness = 20 Å, and 300 kV accelerating voltage. The simulations indicate that the oxygen atoms become visible at appropriate defocus values (~ 2 to 4 nm) and reasonable specimen thicknesses (below 12.25 nm), which is similar to the experimental oxygen imaging conditions (Materials and Methods).

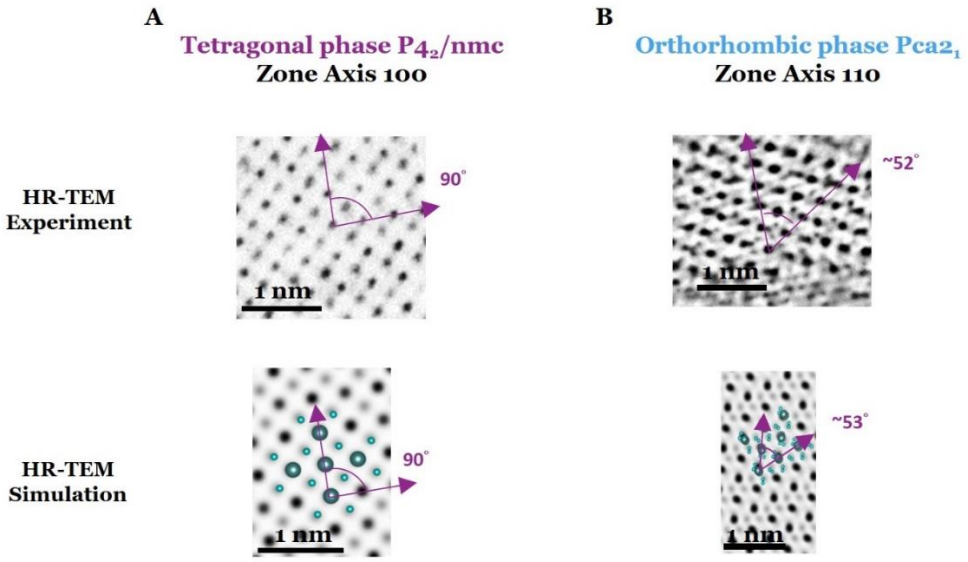

Fig. S7. Ferroic phase identification from lattice angle analysis. (**A**) Experimental HR-TEM imaging of 5 nm ZrO_2 (top) matches the expected cation-cation bond angle along the [001] projection of the tetragonal *P*4$_2$*/nmc* structure (bottom). (**B**) Experimental HR-TEM imaging of 2 nm ZrO_2 (top) matches the expected cation-cation bond angle along the [110] projection of the orthorhombic *Pca*2$_1$ structure (bottom). The slight angle deviation may be possibly due to distorted regions present in the thin sample specimen. The simulations in (A) and (B) implemented the following conditions: specimen thickness ~ 9.8 nm and defocus = 4 nm (Materials and Methods).

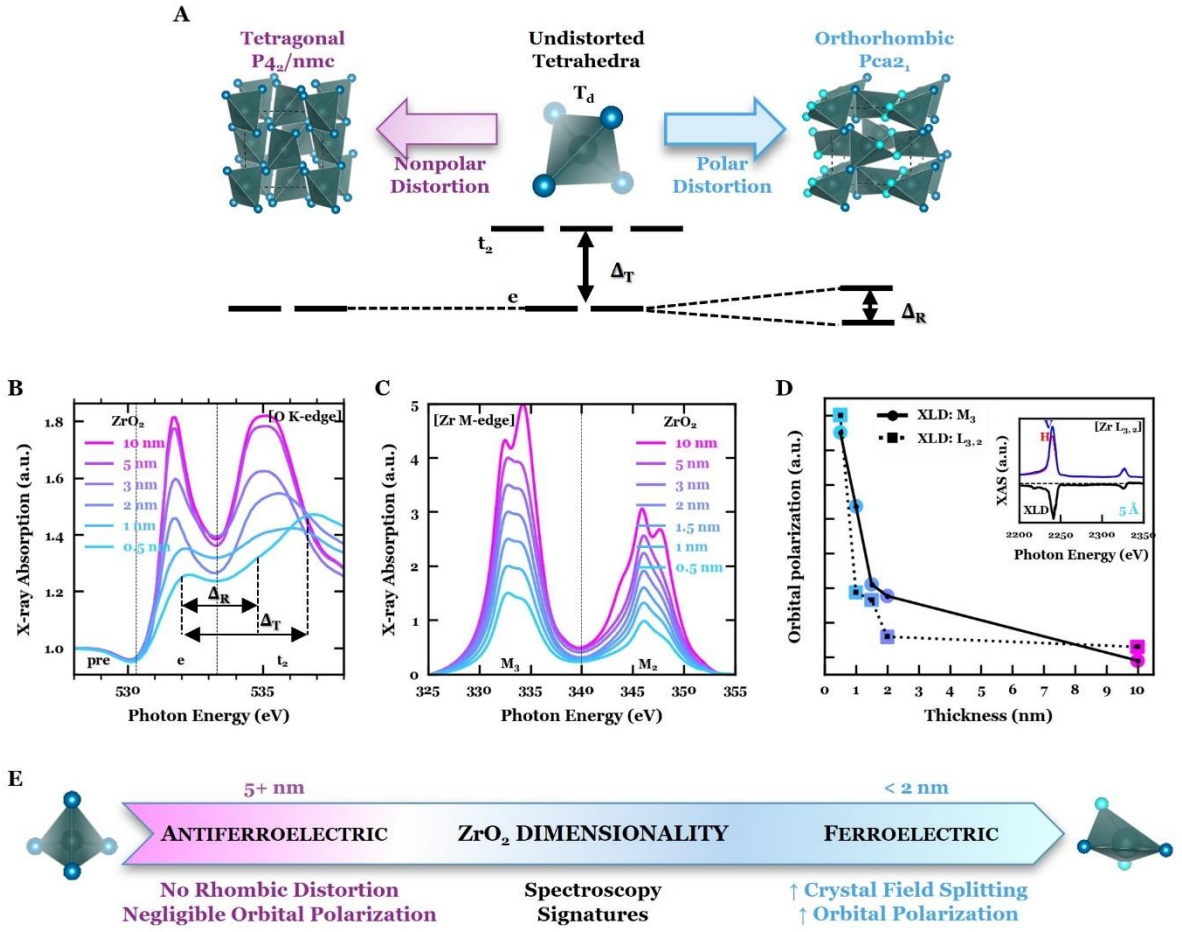

Fig. S8. Ferroic phase insights from synchrotron X-ray spectroscopy. (**A**) Crystal field splitting diagram for tetragonal and orthorhombic phases. Symmetry-induced *e*-manifold splitting can provide a spectroscopic signature of polar orthorhombic phase (Supplementary Text). (**B**) Thickness dependent XAS spectra at the oxygen *K*-edge, indicating the pronounced presence of the polar rhombic distortion, indicative of the ferroelectric o-phase, in ultrathin ZrO_2 films. (**C**) Thickness-dependent XAS spectra at the Zr $M_{3,2}$-edge; the crystal field features present underlie the presence of crystalline ZrO_2 films down to the atomic-scale limit. (**D**) Extracted orbital polarization – indicative of polarization (Supplementary Text) – from XLD measurements at the Zr $M_{3,2}$-edge and Zr $L_{3,2}$-edge as a function of ZrO_2 thickness; the ultrathin-enhanced orbital polarization is likely due to the increased ferroelectric phase emergence and polar distortion present in thinner ZrO_2 films (Fig. 1, 2). Inset: linear polarization-dependent XAS (red, blue) and XLD (black) of 5 Å ZrO_2 at the Zr-$L_{3,2}$-edge. (**E**) Dimensionality-driven evolution of ZrO_2 from the antiferroelectric tetragonal phase to the ferroelectric orthorhombic phase demonstrated through structural signatures in X-ray spectroscopy.

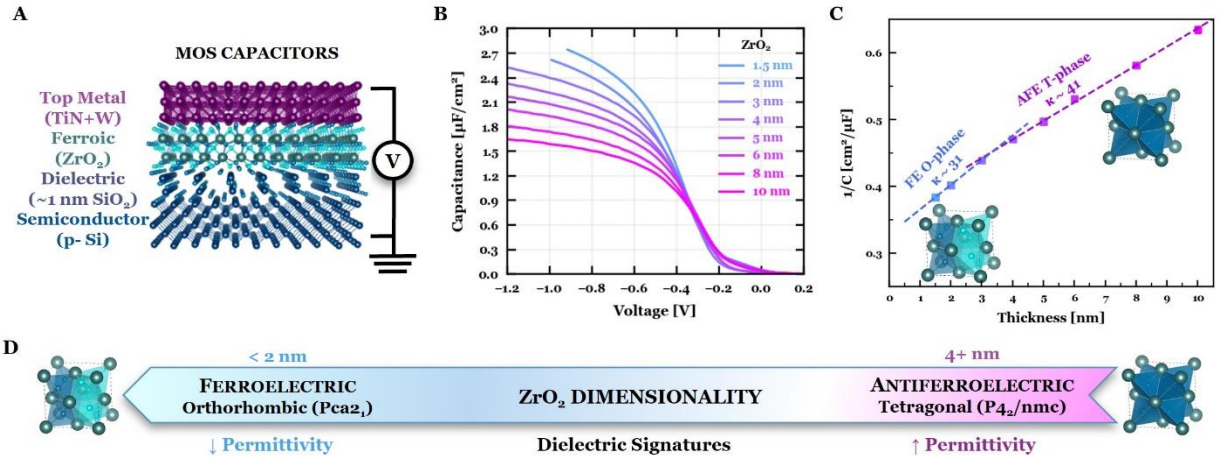

Fig. S9. Ferroic phase insights from dielectric measurements. (**A**) Schematic of MOS capacitors used for accumulation *C-V* measurements. (**B**) *C-V* measurements of ZrO_2 thickness series in MOS capacitors. (**C**) Extracted permittivity (κ) from ZrO_2 thickness-dependent MOS *C-V* measurements. The extracted permittivity crosses over from antiferroelectric t-phase permittivity in relatively thick regime (4+ nm) – $\kappa \sim 40$ (*4*) – towards more ferroelectric-like o-phase permittivity – $\kappa \sim 30$ (*4,21*) – for ultrathin ZrO_2 films. (**D**) Dimensionality-driven evolution of ZrO_2 from the antiferroelectric tetragonal phase to the ferroelectric orthorhombic phase demonstrated through dielectric measurements.

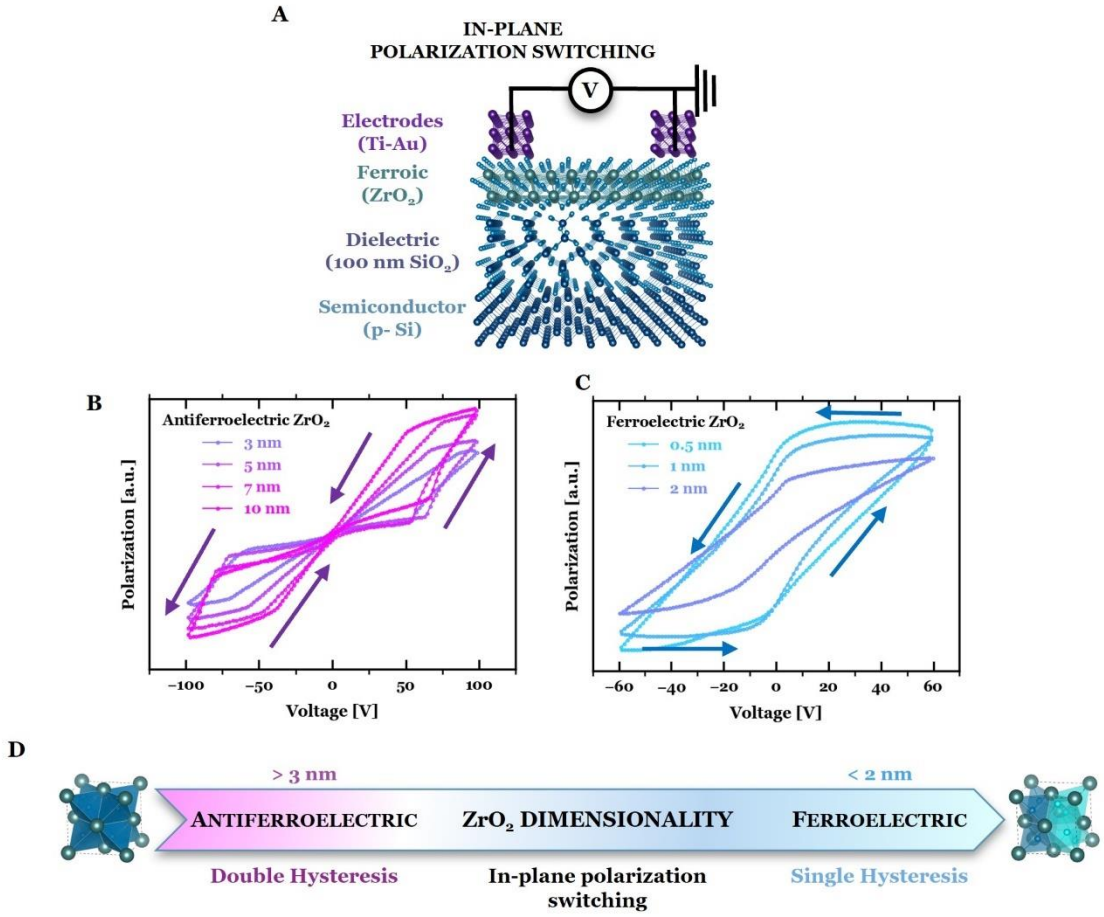

Fig. S10. Ferroic phase insights from in-plane polarization-voltage loops. (**A**) Schematic of the in-plane device structures used for in-plane polarization-voltage (*P*-*V*) loops. (**B**) Antiferroelectric-like counter-clockwise double hysteresis *P*-*V* behavior for relatively thick (3, 5, 7, 10 nm) ZrO_2. (**C**) Ferroelectric-like counter-clockwise hysteresis *P*-*V* behavior for ultrathin (2, 1, 0.5 nm) ZrO_2 films. Note the slightly pinched *P*-*V* behavior for 2 nm ZrO_2 is consistent with the structural trends indicating 2 nm is around the AFE-to-FE phase transition point. (**D**) Dimensionality-driven evolution of ZrO_2 from the antiferroelectric-to-ferroelectric phase demonstrated through polarization switching.

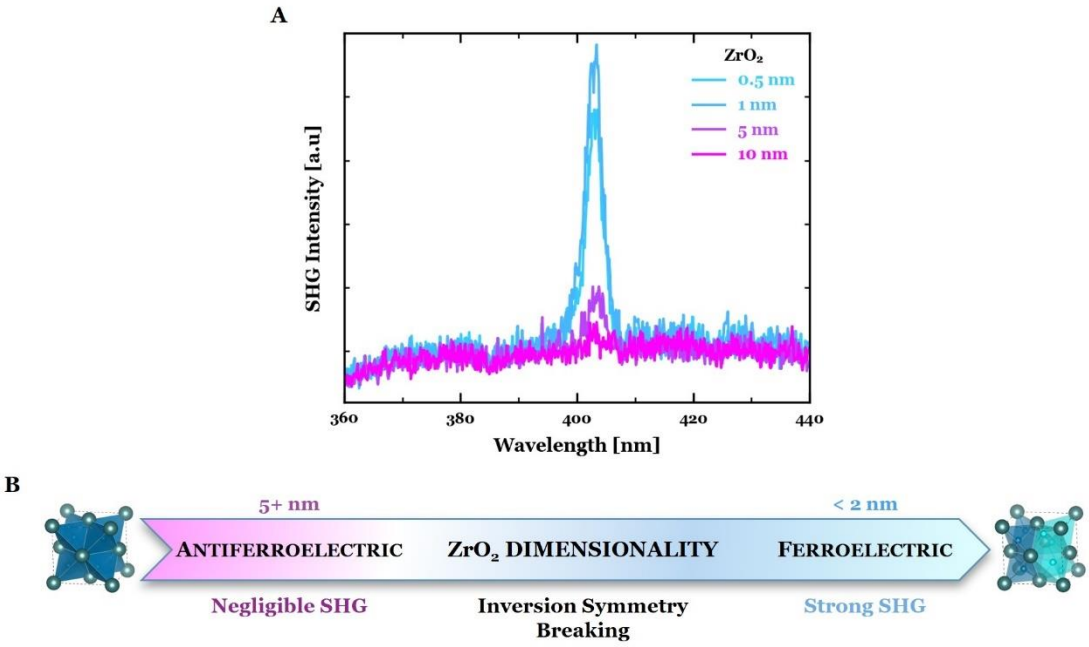

Fig. S11. Second harmonic generation (SHG) spectra. (**A**) SHG spectrum for ultrathin (0.5 nm, 1 nm) ferroelectric ZrO_2 films and relatively thick (5 nm, 10 nm) antiferroelectric ZrO_2 films, which demonstrate strong and negligible SHG intensity around 405 nm (810 nm fundamental laser beam), respectively, consistent with the SHG mapping trends (Fig. 2C). (**B**) Dimensionality-driven evolution of ZrO_2 from the nonpolar antiferroelectric phase to the polar ferroelectric phase indicated by inversion symmetry breaking.

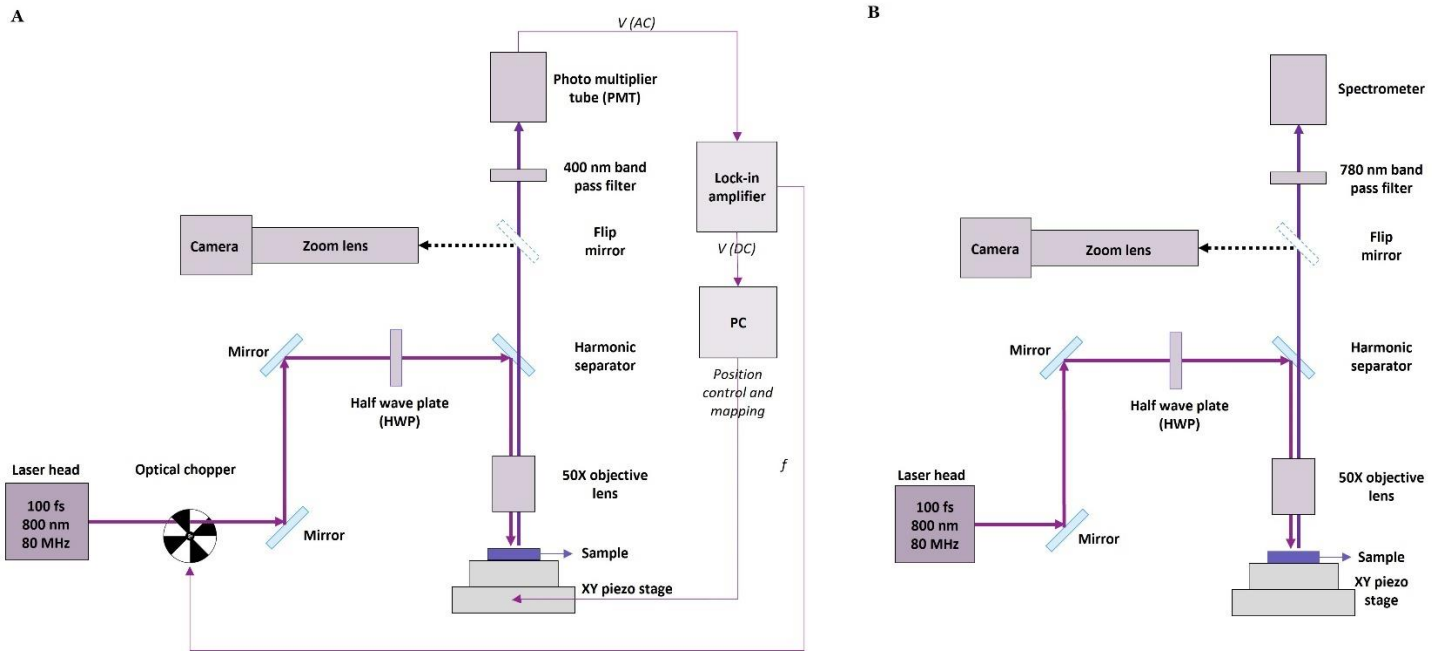

Fig. S12. Second harmonic generation (SHG) measurement setups. (**A, B**) Schematics for the spatially-resolved SHG (A, Fig. 2C) and emission spectrum SHG (B, fig. S11) setups used to probe in-plane symmetry breaking (Supplementary Text) in ZrO_2 films.

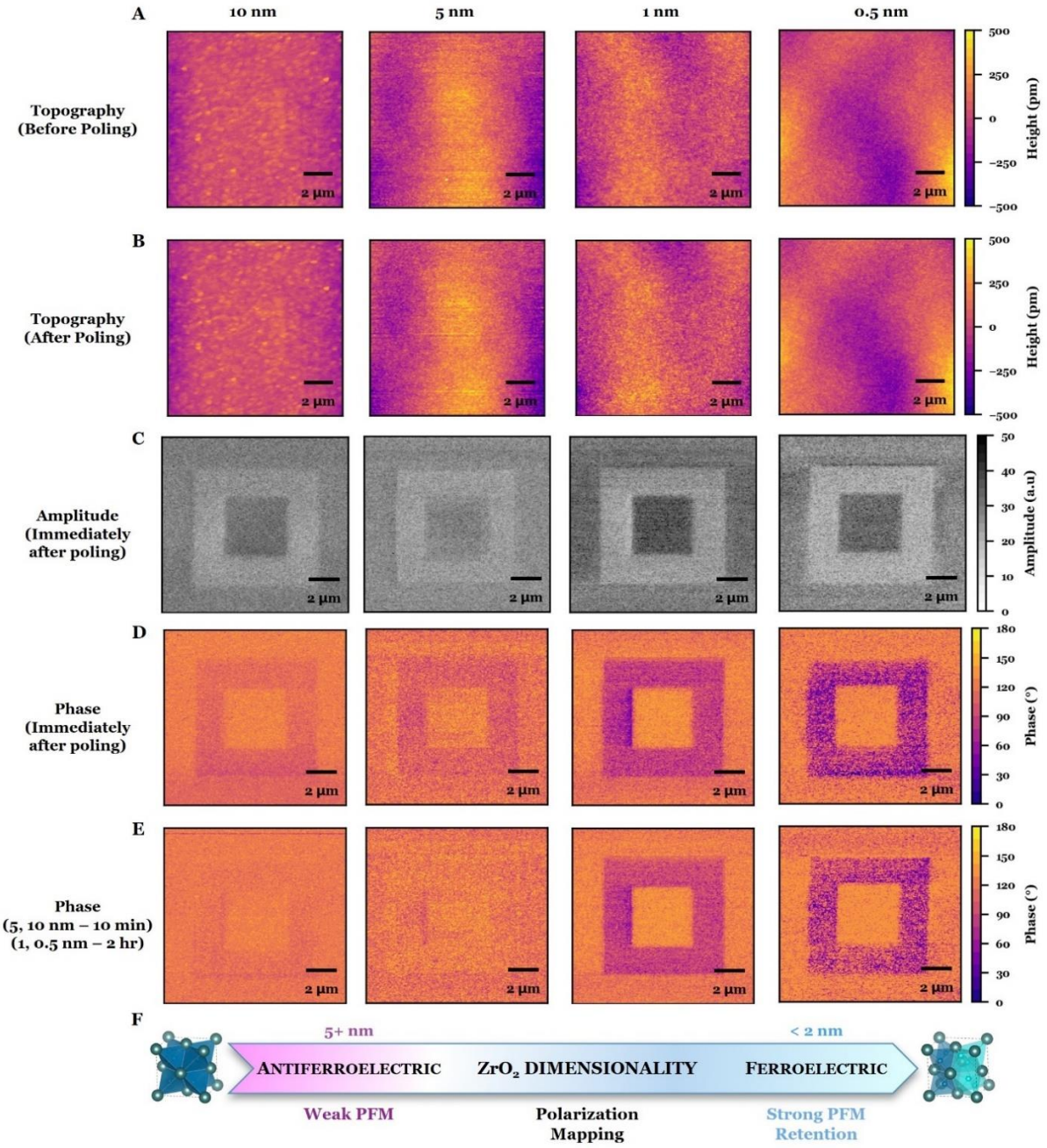

Fig. S13. Ferroic phase insights from scanning probe microscopy. (**A, B**) AFM topography before (A) and after (B) poling a box-in-box pattern onto ZrO_2 films of various thickness, demonstrating no topographic change to the ZrO_2 surface due to poling. The inner (outer) box was poled with positive (negative) bias. (**C, D)** PFM amplitude (C) and phase (D) images after poling a box-in-box pattern, demonstrating minimal contrast for relatively thick (5, 10 nm) ZrO_2 and strong contrast for ultrathin (0.5, 1 nm) ZrO_2. (**E**) Retention of PFM phase contrast. The weak contrast in relatively thick (5, 10 nm) ZrO_2 vanishes within 10 minutes; meanwhile, the strong contrast present in ultrathin (0.5, 1 nm) ZrO_2 remains after 2 hours, indicating long-term persistence of the ferroelectric polarization. (**F**) Dimensionality-driven antiferroelectric-to-ferroelectric evolution of ZrO_2 illustrated through polarization mapping.

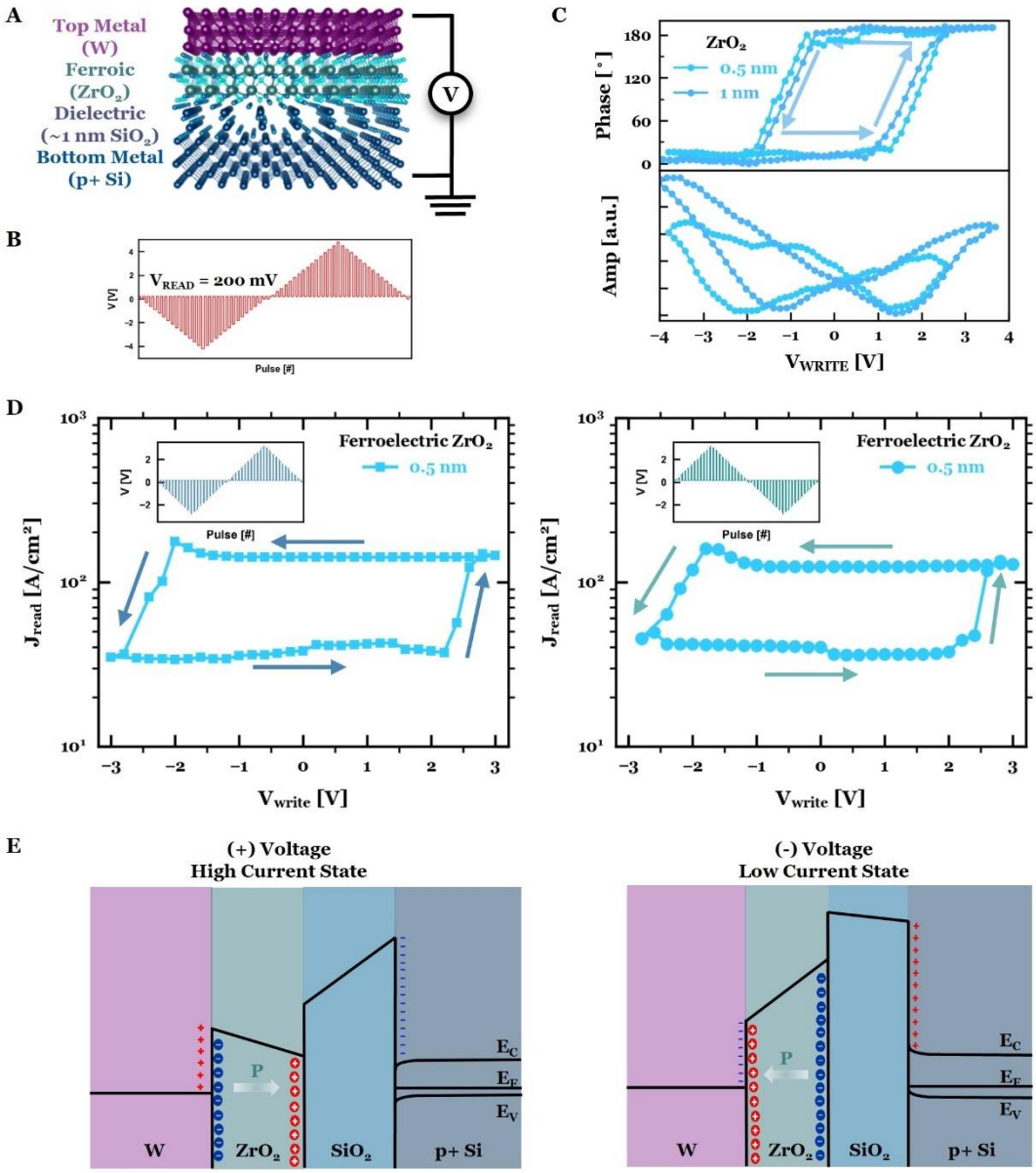

Fig. S14. Ferroic phase insights from field-dependent hysteretic measurements. (**A**) Schematic of metal-ferroic-insulator-semiconductor (MFIS) ferroic tunnel junction. (**B**) Voltage waveform used in pulsed *I-V* and PFM measurements. (**C**) PFM spectroscopy hysteresis loops for ultrathin (5 Å and 1 nm) ZrO_2; the 180 ° phase hysteretic behavior and butterfly-shaped amplitude loops are consistent with FE-like polarization switching. (**D**) Pulsed current-voltage (I-V_{write}) hysteresis map as a function of write voltage measured at 200 mV read voltage for ultrathin (5 Å) ZrO_2, consistent with FE-like polarization switching based on the counter-clockwise hysteresis sense (E). The abrupt hysteretic behavior and saturating tunnelling electroresistance is characteristic of polarization-driven switching, as opposed to filamentary-based switching mediated by electrochemical migration (Supplementary Text). The ultrathin FTJ devices demonstrates voltage polarity-independent I-V_{write} hysteresis sense: both negative-positive-negative voltage polarity (left, blue) and positive-negative-positive voltage polarity (right, green) demonstrate counterclockwise hysteresis. The voltage polarity-dependent *I-V* hysteresis measurements further

rule out filamentary-based resistive switching mechanisms and is consistent with polarization-driven switching (Supplementary Text). Insets: Voltage waveform used in the pulsed $I\text{-}V_{write}$ measurements; the alternating sequence – staircase write, fixed read – mimics the PFM waveform. (**E**) Electronic band diagrams of the MFIS tunnel junction corresponding to the high-current (left) and low-current (right) states, depending on the remnant polarization in ZrO_2. The high-current state (positive voltage applied to the W, ZrO_2 polarization points away from W) corresponds to a lower average tunneling barrier, and vice-versa for the low-current state. The uncircled '+' and '-' symbols in the metal and semiconductor represent holes and electrons, respectively, while the circled '+' and '-' symbols in the ferroic layer represent the dipole charges in the ferroic. In the band diagrams it is assumed that the ferroic bound charges at the metal/ferroic interface are perfectly screened and therefore the barrier height at the metal/ferroic interface is fixed and independent of polarization direction.

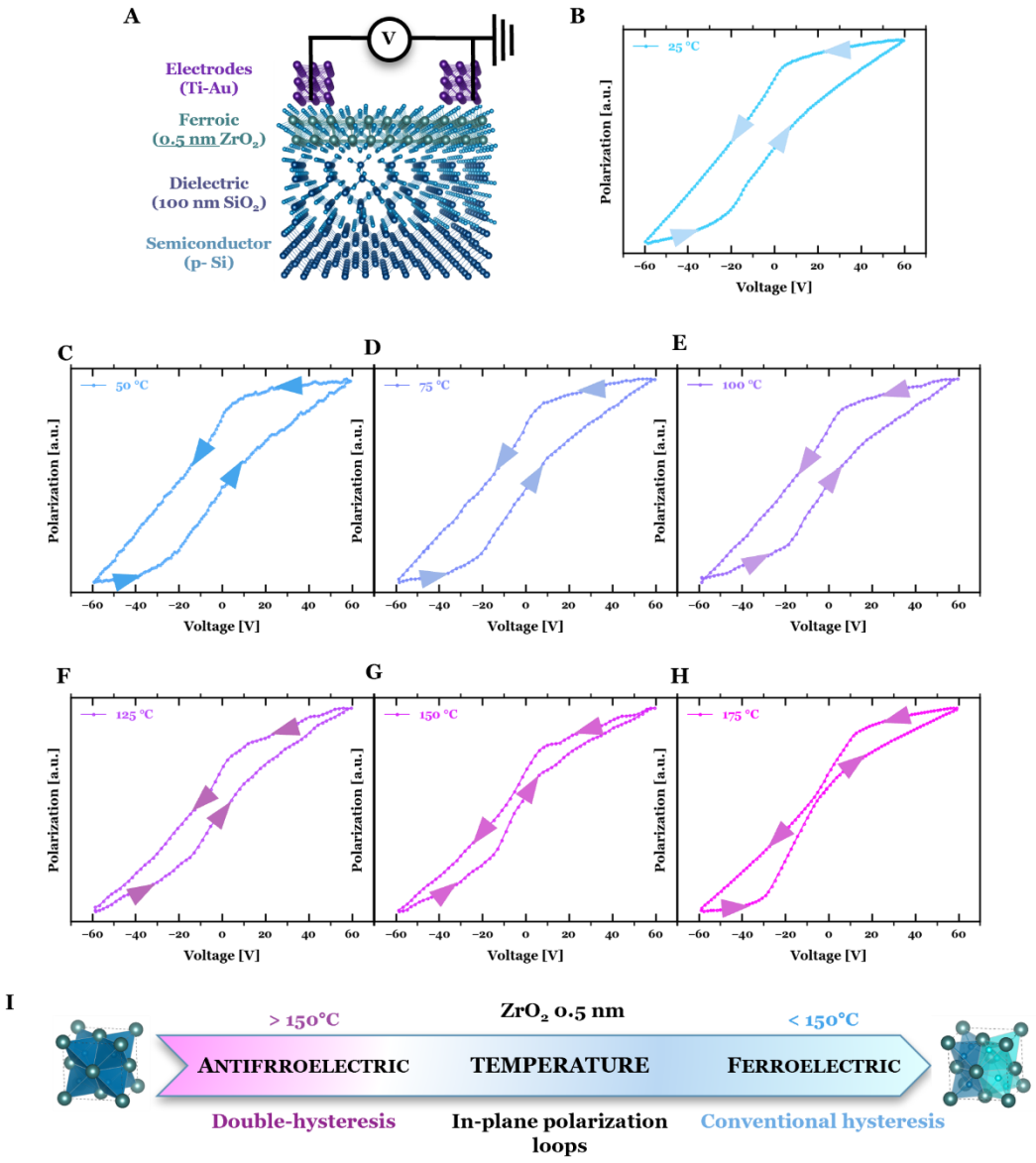

Fig. S15. Temperature-dependent ferroelectric-antiferroelectric phase transition in 0.5 nm ZrO_2. (**A**) Schematic of the in-plane device structures used for temperature-dependent in-plane polarization-voltage (*P-V*) loops for 0.5 nm ZrO_2 films. (**B,C,D,E,F,G,H**) *P-V* loops from 25°C to 175°C in 25°C increments, starting with ferroelectric-like hysteresis at 25°C. The *P-V* loops become more pinched with increasing temperature until finally demonstrating complete antiferroelectric-like double hysteresis switching at 175°C. The Curie temperature is ~ 150°C, well above room temperature. (**I**) Temperature-dependent antiferroelectric-to-ferroelectric phase evolution in 0.5 nm ZrO_2 demonstrated through polarization switching.

References and Notes

1. S. Salahuddin, K. Ni, S. Datta, The era of hyper-scaling in electronics. *Nat. Electron.* **1**, 442–450 (2018). doi:10.1038/s41928-018-0117-x

2. M. Dawber, K. M. Rabe, J. F. Scott, Physics of thin-film ferroelectric oxides. *Rev. Mod. Phys.* **77**, 1083–1130 (2005). doi:10.1103/RevModPhys.77.1083

3. T. S. Böscke, J. Müller, D. Bräuhaus, U. Schröder, U. Böttger, Ferroelectricity in hafnium oxide thin films. *Appl. Phys. Lett.* **99**, 102903 (2011). doi:10.1063/1.3634052

4. J. Müller, T. S. Böscke, U. Schröder, S. Mueller, D. Bräuhaus, U. Böttger, L. Frey, T. Mikolajick, Ferroelectricity in simple binary ZrO_2 and HfO_2. *Nano Lett.* **12**, 4318–4323 (2012). doi:10.1021/nl302049k Medline

5. T. Mikolajick, U. Schroeder, M. H. Park, Special topic on ferroelectricity in hafnium oxide: Materials and devices. *Appl. Phys. Lett.* **118**, 180402 (2021). doi:10.1063/5.0054064

6. H. Qiao, C. Wang, W. S. Choi, M. H. Park, Y. Kim, Ultra-thin ferroelectrics. *Mater. Sci. Eng. Rep.* **145**, 100622 (2021). doi:10.1016/j.mser.2021.100622

7. J. F. Ihlefeld, D. T. Harris, R. Keech, J. L. Jones, J.-P. Maria, S. Trolier-McKinstry, Scaling effects in perovskite ferroelectrics: Fundamental limits and process-structure-property relations. *J. Am. Ceram. Soc.* **99**, 2537–2557 (2016). doi:10.1111/jace.14387

8. T. Mikolajick, S. Slesazeck, H. Mulaosmanovic, M. H. Park, S. Fichtner, P. D. Lomenzo, M. Hoffmann, U. Schroeder, Next generation ferroelectric materials for semiconductor process integration and their applications. *J. Appl. Phys.* **129**, 100901 (2021). doi:10.1063/5.0037617

9. U. Schroeder, M. Materano, T. Mittmann, P. D. Lomenzo, T. Mikolajick, A. Toriumi, Recent progress for obtaining the ferroelectric phase in hafnium oxide based films: Impact of oxygen and zirconium. *Jpn. J. Appl. Phys.* **58**, SL0801 (2019). doi:10.7567/1347-4065/ab45e3

10. Y. Wei, P. Nukala, M. Salverda, S. Matzen, H. J. Zhao, J. Momand, A. S. Everhardt, G. Agnus, G. R. Blake, P. Lecoeur, B. J. Kooi, J. Íñiguez, B. Dkhil, B. Noheda, A rhombohedral ferroelectric phase in epitaxially strained $Hf_{0.5}Zr_{0.5}O_2$ thin films. *Nat. Mater.* **17**, 1095–1100 (2018). doi:10.1038/s41563-018-0196-0 Medline

11. S. S. Cheema, D. Kwon, N. Shanker, R. Dos Reis, S.-L. Hsu, J. Xiao, H. Zhang, R. Wagner, A. Datar, M. R. McCarter, C. R. Serrao, A. K. Yadav, G. Karbasian, C.-H. Hsu, A. J. Tan, L.-C. Wang, V. Thakare, X. Zhang, A. Mehta, E. Karapetrova, R. V. Chopdekar, P. Shafer, E. Arenholz, C. Hu, R. Proksch, R. Ramesh, J. Ciston, S. Salahuddin, Enhanced ferroelectricity in ultrathin films grown directly on silicon. *Nature* **580**, 478–482 (2020). doi:10.1038/s41586-020-2208-x Medline

12. H.-J. Lee, M. Lee, K. Lee, J. Jo, H. Yang, Y. Kim, S. C. Chae, U. Waghmare, J. H. Lee, Scale-free ferroelectricity induced by flat phonon bands in HfO_2. *Science* **369**, 1343–1347 (2020). doi:10.1126/science.aba0067 Medline

13. B. Noheda, J. Íñiguez, A key piece of the ferroelectric hafnia puzzle. *Science* **369**, 1300–1301 (2020). doi:10.1126/science.abd1212 Medline

14. M. Dogan, S. Fernandez-Peña, L. Kornblum, Y. Jia, D. P. Kumah, J. W. Reiner, Z. Krivokapic, A. M. Kolpak, S. Ismail-Beigi, C. H. Ahn, F. J. Walker, Single atomic layer ferroelectric on silicon. *Nano Lett.* **18**, 241–246 (2018). doi:10.1021/acs.nanolett.7b03988 Medline

15. O. Ohtaka, H. Fukui, T. Kunisada, T. Fujisawa, K. Funakoshi, W. Utsumi, T. Irifune, K. Kuroda, T. Kikegawa, Phase relations and equations of state of ZrO_2 under high temperature and high pressure. *Phys. Rev. B* **63**, 174108 (2001). doi:10.1103/PhysRevB.63.174108

16. T. Song, H. Tan, N. Dix, R. Moalla, J. Lyu, G. Saint-Girons, R. Bachelet, F. Sánchez, I. Fina, Stabilization of the ferroelectric phase in epitaxial $Hf_{1-x}Zr_xO_2$ enabling coexistence of ferroelectric and enhanced piezoelectric properties. *ACS Appl. Electron. Mater.* **3**, 2106–2113 (2021). doi:10.1021/acsaelm.1c00122

17. C. A. Randall, Z. Fan, I. Reaney, L. Chen, S. Trolier-McKinstry, Antiferroelectrics: History, fundamentals, crystal chemistry, crystal structures, size effects, and applications. *J. Am. Ceram. Soc.* **104**, 3775–3810 (2021). doi:10.1111/jace.17834

18. Materials, methods, and additional information are available as supplementary materials.

19. P. Nukala, M. Ahmadi, Y. Wei, S. de Graaf, E. Stylianidis, T. Chakrabortty, S. Matzen, H. W. Zandbergen, A. Björling, D. Mannix, D. Carbone, B. Kooi, B. Noheda, Reversible oxygen migration and phase transitions in hafnia-based ferroelectric devices. *Science* **372**, 630–635 (2021). doi:10.1126/science.abf3789 Medline

20. H. Du, C. Groh, C.-L. Jia, T. Ohlerth, R. E. Dunin-Borkowski, U. Simon, J. Mayer, Multiple polarization orders in individual twinned colloidal nanocrystals of centrosymmetric HfO_2. *Matter* **4**, 986–1000 (2021). doi:10.1016/j.matt.2020.12.008

21. R. Materlik, C. Künneth, A. Kersch, The origin of ferroelectricity in $Hf_{1-x}Zr_xO_2$: A computational investigation and a surface energy model. *J. Appl. Phys.* **117**, 134109 (2015). doi:10.1063/1.4916707

22. Y. Wei, S. Matzen, T. Maroutian, G. Agnus, M. Salverda, P. Nukala, Q. Chen, J. Ye, B. Lecoeur, B. Noheda, Magnetic tunnel junctions based on ferroelectric $Hf_{0.5}Zr_{0.5}O_2$ tunnel barriers. *Phys. Rev. Appl.* **12**, 031001 (2019). doi:10.1103/PhysRevApplied.12.031001

23. S. S. Cheema, N. Shanker, C.-H. Hsu, A. Datar, J. Bae, D. Kwon, S. Salahuddin, One nanometer HfO_2-based ferroelectric tunnel junctions on silicon. *Adv. Electron. Mater.* 10.1002/aelm.202100499 (2021). doi:10.1002/aelm.202100499

24. S. E. Reyes-Lillo, K. F. Garrity, K. M. Rabe, Antiferroelectricity in thin-film ZrO_2 from first principles. *Phys. Rev. B* **90**, 140103 (2014). doi:10.1103/PhysRevB.90.140103

25. W. J. Merz, The effect of hydrostatic pressure on the curie point of barium titanate single crystals. *Phys. Rev.* **78**, 52–54 (1950). doi:10.1103/PhysRev.78.52

26. J. Lyu, I. Fina, R. Solanas, J. Fontcuberta, F. Sánchez, Growth window of ferroelectric epitaxial $Hf_{0.5}Zr_{0.5}O_2$ thin films. *ACS Appl. Electron. Mater.* **1**, 220–228 (2019). doi:10.1021/acsaelm.8b00065

27. J. Liu, S. Liu, J.-Y. Yang, L. Liu, Electric auxetic effect in piezoelectrics. *Phys. Rev. Lett.* **125**, 197601 (2020). doi:10.1103/PhysRevLett.125.197601 Medline

28. N. Sai, C. J. Fennie, A. A. Demkov, Absence of critical thickness in an ultrathin improper ferroelectric film. *Phys. Rev. Lett.* **102**, 107601 (2009). doi:10.1103/PhysRevLett.102.107601 Medline

29. J. Junquera, P. Ghosez, Critical thickness for ferroelectricity in perovskite ultrathin films. *Nature* **422**, 506–509 (2003). doi:10.1038/nature01501 Medline

30. D. Lee, H. Lu, Y. Gu, S.-Y. Choi, S.-D. Li, S. Ryu, T. R. Paudel, K. Song, E. Mikheev, S. Lee, S. Stemmer, D. A. Tenne, S. H. Oh, E. Y. Tsymbal, X. Wu, L.-Q. Chen, A. Gruverman, C. B. Eom, Emergence of room-temperature ferroelectricity at reduced dimensions. *Science* **349**, 1314–1317 (2015). doi:10.1126/science.aaa6442 Medline

31. M. P. Warusawithana, C. Cen, C. R. Sleasman, J. C. Woicik, Y. Li, L. F. Kourkoutis, J. A. Klug, H. Li, P. Ryan, L. P. Wang, M. Bedzyk, D. A. Muller, L. Q. Chen, J. Levy, D. G. Schlom, A ferroelectric oxide made directly on silicon. *Science* **324**, 367–370 (2009). doi:10.1126/science.1169678 Medline

32. J. H. Haeni, P. Irvin, W. Chang, R. Uecker, P. Reiche, Y. L. Li, S. Choudhury, W. Tian, M. E. Hawley, B. Craigo, A. K. Tagantsev, X. Q. Pan, S. K. Streiffer, L. Q. Chen, S. W. Kirchoefer, J. Levy, D. G. Schlom, Room-temperature ferroelectricity in strained $SrTiO_3$. *Nature* **430**, 758–761 (2004). doi:10.1038/nature02773 Medline

33. E. Tsymbal, Two-dimensional ferroelectricity by design. *Science* **372**, 1389–1390 (2021). doi:10.1126/science.abi7296

34. R. Batra, H. D. Tran, B. Johnson, B. Zoellner, P. A. Maggard, J. L. Jones, G. A. Rossetti Jr., R. Ramprasad, Search for ferroelectric binary oxides: Chemical and structural space exploration guided by group theory and computations. *Chem. Mater.* **32**, 3823–3832 (2020). doi:10.1021/acs.chemmater.9b05324

35. R. W. Johnson, A. Hultqvist, S. F. Bent, A brief review of atomic layer deposition: From fundamentals to applications. *Mater. Today* **17**, 236–246 (2014). doi:10.1016/j.mattod.2014.04.026

36. K. W. Urban, C. L. Jia, L. Houben, M. Lentzen, S. B. Mi, K. Tillmann, Negative spherical aberration ultrahigh-resolution imaging in corrected transmission electron microscopy. *Philos. Trans. A Math. Phys. Eng. Sci.* **367**, 3735–3753 (2009). doi:10.1098/rsta.2009.0134 Medline

37. A. Pryor Jr., C. Ophus, J. Miao, A streaming multi-GPU implementation of image simulation algorithms for scanning transmission electron microscopy. *Adv. Struct. Chem. Imaging* **3**, 15 (2017). doi:10.1186/s40679-017-0048-z Medline

38. C. Ophus, A fast image simulation algorithm for scanning transmission electron microscopy. *Adv. Struct. Chem. Imaging* **3**, 13 (2017). doi:10.1186/s40679-017-0046-1 Medline

39. B. J. Rodriguez, C. Callahan, S. V. Kalinin, R. Proksch, Dual-frequency resonancetracking atomic force microscopy. *Nanotechnology* **18**, 475504 (2007). doi:10.1088/0957-4484/18/47/475504

40. S. Jesse, H. N. Lee, S. V. Kalinin, Quantitative mapping of switching behavior in piezoresponse force microscopy. *Rev. Sci. Instrum.* **77**, 073702 (2006). doi:10.1063/1.2214699

41. S. Hong, J. Woo, H. Shin, J. Jeon, E. Y. Pak, E. L. Colla, N. Setter, E. Kim, K. No, Principle of ferroelectric domain imaging using atomic force microscope. *J. Appl. Phys.* **89**, 1377–1386 (2001). doi:10.1063/1.1331654

42. R. K. Vasudevan, N. Balke, P. Maksymovych, S. Jesse, S. V. Kalinin, Ferroelectric or non-ferroelectric: Why so many materials exhibit "ferroelectricity" on the nanoscale. *Appl. Phys. Rev.* **4**, 021302 (2017). doi:10.1063/1.4979015

43. M. Björck, G. Andersson, GenX: An extensible x-ray reflectivity refinement program utilizing differential evolution. *J. Appl. Cryst.* **40**, 1174–1178 (2007). doi:10.1107/S0021889807045086

44. J. Ilavsky, Nika: Software for two-dimensional data reduction. *J. Appl. Cryst.* **45**, 324–328 (2012). doi:10.1107/S0021889812004037

45. H. A. Hsain, Y. Lee, G. Parsons, J. L. Jones, Compositional dependence of crystallization temperatures and phase evolution in hafnia-zirconia $(Hf_xZr_{1-x})O_2$ thin films. *Appl. Phys. Lett.* **116**, 192901 (2020). doi:10.1063/5.0002835

46. A. T. Young, E. Arenholz, S. Marks, R. Schlueter, C. Steier, H. A. Padmore, A. P. Hitchcock, D. G. Castner, Variable linear polarization from an x-ray undulator. *J. Synchrotron Radiat.* **9**, 270–274 (2002). doi:10.1107/S0909049502007161 Medline

47. K. Yang, C. Hu, MOS capacitance measurements for high-leakage thin dielectrics. *IEEE Trans. Electron Dev.* **46**, 1500–1501 (1999). doi:10.1109/16.772500

48. E. D. Grimley, J. M. LeBeau, "Transmission electron microscopy (STEM and TEM)" in *Ferroelectricity in Doped Hafnium Oxide: Materials, Properties and Devices*, U. Schroeder, C. S. Hwang, H. Funakubo, Eds. (Elsevier, 2019), pp. 317–340.

49. X. Sang, E. D. Grimley, T. Schenk, U. Schroeder, J. M. LeBeau, On the structural origins of ferroelectricity in HfO_2 thin films. *Appl. Phys. Lett.* **106**, 162905 (2015). doi:10.1063/1.4919135

50. P. Nukala, J. Antoja-Lleonart, Y. Wei, L. Yedra, B. Dkhil, B. Noheda, Direct epitaxial growth of polar $(1-x)HfO_2-(x)ZrO_2$ ultrathin films on silicon. *ACS Appl. Electron. Mater.* **1**, 2585–2593 (2019). doi:10.1021/acsaelm.9b00585 Medline

51. J. M. LeBeau, A. J. D'Alfonso, N. J. Wright, L. J. Allen, S. Stemmer, Determining ferroelectric polarity at the nanoscale. *Appl. Phys. Lett.* **98**, 052904 (2011). doi:10.1063/1.3549300

52. P. Nukala, M. Ahmadi, J. Antoja-Lleonart, S. de Graaf, Y. Wei, H. W. Zandbergen, B. J. Kooi, B. Noheda, In situ heating studies on temperature-induced phase transitions in epitaxial $Hf_{0.5}Zr_{0.5}O_2/La_{0.67}Sr_{0.33}MnO_3$ heterostructures. *Appl. Phys. Lett.* **118**, 062901 (2021). doi:10.1063/5.0035714

53. Q. Luo, Y. Cheng, J. Yang, R. Cao, H. Ma, Y. Yang, R. Huang, W. Wei, Y. Zheng, T. Gong, J. Yu, X. Xu, P. Yuan, X. Li, L. Tai, H. Yu, D. Shang, Q. Liu, B. Yu, Q. Ren, H. Lv, M. Liu, A highly CMOS compatible hafnia-based ferroelectric diode. *Nat. Commun.* **11**, 1391 (2020). doi:10.1038/s41467-020-15159-2 Medline

54. C. L. Jia, M. Lentzen, K. Urban, Atomic-resolution imaging of oxygen in perovskite ceramics. *Science* **299**, 870–873 (2003). doi:10.1126/science.1079121 Medline

55. C. Jia, L. Houben, A. Thust, J. Barthel, On the benefit of the negative-spherical-aberration imaging technique for quantitative HRTEM. *Ultramicroscopy* **110**, 500–505 (2010). doi:10.1016/j.ultramic.2009.10.006

56. M. H. Park, Y. H. Lee, H. J. Kim, Y. J. Kim, T. Moon, K. D. Kim, J. Müller, A. Kersch, U. Schroeder, T. Mikolajick, C. S. Hwang, Ferroelectricity and antiferroelectricity of doped thin HfO_2-based films. *Adv. Mater.* **27**, 1811–1831 (2015). doi:10.1002/adma.201404531 Medline

57. F. Mehmood, T. Mikolajick, U. Schroeder, Lanthanum doping induced structural changes and their implications on ferroelectric properties of $Hf_{1-x}Zr_xO_2$ thin film. *Appl. Phys. Lett.* **117**, 092902 (2020). doi:10.1063/5.0021007

58. N. Tasneem, Y. M. Yousry, M. Tian, M. Dopita, S. E. Reyes-Lillo, J. Kacher, N. Bassiri-Gharb, A. I. Khan, A Janovec-Kay-Dunn-like behavior at thickness scaling in ultra-thin antiferroelectric ZrO_2 films. *Adv. Electron. Mater.* **7**, 2100485 (2021). doi:10.1002/aelm.202100485

59. M. H. Park, T. Schenk, C. Fancher, E. Grimley, C. Zhou, C. Richter, J. M. LeBeau, J. L. Jones, T. Mikolajick, U. Schroeder, A comprehensive study on the structural evolution of HfO_2 thin films doped with various dopants. *J. Mater. Chem. C Mater. Opt. Electron. Devices* **5**, 4677–4690 (2017). doi:10.1039/C7TC01200D

60. C. Lichtensteiger, M. Dawber, J.-M. Triscone, "Ferroelectric size effects" in *Physics of Ferroelectrics: A Modern Perspective*, K. M. Rabe, C. H. Ahn, J.-M. Triscone, Eds. (Topics in Applied Physics Series, vol. 105, Springer, 2007), pp. 305–338.

61. P. D. Lomenzo, M. Materano, T. Mittmann, P. Buragohain, A. Gruverman, T. Kiguchi, T. Mikolajick, U. Schroeder, Harnessing phase transitions in antiferroelectric ZrO_2 Using the size effect. *Adv. Electron. Mater.* **8**, 202100556 (2021). doi:10.1002/aelm.202100556

62. D. M. Smilgies, Scherrer grain-size analysis adapted to grazing-incidence scattering with area detectors. *J. Appl. Crystallogr.* **42**, 1030–1034 (2009). doi:10.1107/S0021889809040126 Medline

63. D.-Y. Cho, H.-S. Jung, C. S. Hwang, Structural properties and electronic structure of HfO_2-ZrO_2 composite films. *Phys. Rev. B* **82**, 094104 (2010). doi:10.1103/PhysRevB.82.094104

64. A. Jain, S. P. Ong, G. Hautier, W. Chen, W. D. Richards, S. Dacek, S. Cholia, D. Gunter, D. Skinner, G. Ceder, K. A. Persson, The materials project: A materials genome approach to accelerating materials innovation. *APL Mater.* **1**, 011002 (2013). doi:10.1063/1.4812323

65. K. Mathew, C. Zheng, D. Winston, C. Chen, A. Dozier, J. J. Rehr, S. P. Ong, K. A. Persson, High-throughput computational x-ray absorption spectroscopy. *Sci. Data* **5**, 180151 (2018). doi:10.1038/sdata.2018.151 Medline

66. R. E. Cohen, Origin of ferroelectricity in perovskite oxides. *Nature* **358**, 136–138 (1992). doi:10.1038/358136a0

67. D. Pesquera, G. Herranz, A. Barla, E. Pellegrin, F. Bondino, E. Magnano, F. Sánchez, J. Fontcuberta, Surface symmetry-breaking and strain effects on orbital occupancy in transition metal perovskite epitaxial films. *Nat. Commun.* **3**, 1189 (2012). doi:10.1038/ncomms2189 Medline

68. J. F. Ihlefeld, T. S. Luk, S. W. Smith, S. S. Fields, S. T. Jaszewski, D. M. Hirt, W. T. Riffe, S. Bender, C. Constantin, M. V. Ayyasamy, P. V. Balachandran, P. Lu, M. David Henry, P. S. Davids, Compositional dependence of linear and nonlinear optical response in crystalline hafnium zirconium oxide thin films. *J. Appl. Phys.* **128**, 034101 (2020). doi:10.1063/5.0012175

69. J. Scott, J. Gardner, Ferroelectrics, multiferroics and artifacts: Lozenge-shaped hysteresis and things that go bump in the night. *Mater. Today* **21**, 553–562 (2018). doi:10.1016/j.mattod.2017.12.003

70. D. D. Fong, G. B. Stephenson, S. K. Streiffer, J. A. Eastman, O. Auciello, P. H. Fuoss, C. Thompson, Ferroelectricity in ultrathin perovskite films. *Science* **304**, 1650–1653 (2004). doi:10.1126/science.1098252 Medline

71. D. A. Tenne, A. Bruchhausen, N. D. Lanzillotti-Kimura, A. Fainstein, R. S. Katiyar, A. Cantarero, A. Soukiassian, V. Vaithyanathan, J. H. Haeni, W. Tian, D. G. Schlom, K. J. Choi, D. M. Kim, C. B. Eom, H. P. Sun, X. Q. Pan, Y. L. Li, L. Q. Chen, Q. X. Jia, S. M. Nakhmanson, K. M. Rabe, X. X. Xi, Probing nanoscale ferroelectricity by ultraviolet Raman spectroscopy. *Science* **313**, 1614–1616 (2006). doi:10.1126/science.1130306 Medline

72. A. Gruverman, M. Alexe, D. Meier, Piezoresponse force microscopy and nanoferroic phenomena. *Nat. Commun.* **10**, 1661 (2019). doi:10.1038/s41467-019-09650-8 Medline

73. N. G. Orji, M. Badaroglu, B. M. Barnes, C. Beitia, B. D. Bunday, U. Celano, R. J. Kline, M. Neisser, Y. Obeng, A. E. Vladar, Metrology for the next generation of semiconductor devices. *Nat. Electron.* **1**, 532–547 (2018). doi:10.1038/s41928-018-0150-9 Medline

74. F. Hui, M. Lanza, Scanning probe microscopy for advanced nanoelectronics. *Nat. Electron.* **2**, 221–229 (2019). doi:10.1038/s41928-019-0264-8

75. W. Chung, M. Si, P. R. Shrestha, J. P. Campbell, K. P. Cheung, P. D. Ye, "First direct experimental studies of $Hf_{0.5}Zr_{0.5}O_2$ ferroelectric polarization switching down to 100 picosecond in sub-60mV/dec germanium ferroelectric nanowire FETs" in *2018 IEEE Symposium on VLSI Technology* (IEEE, 2018), pp. 89–90.

76. X. Lyu, M. Si, X. Sun, M. A. Capano, H. Wang, P. D. Ye, "Ferroelectric and anti-ferroelectric hafnium zirconium oxide: Scaling limit, switching speed and record high polarization density" in *2019 Symposium on VLSI Technology* (IEEE, 2019), pp. T44–T45.

77. X. Lyu, M. Si, P. R. Shrestha, K. P. Cheung, P. D. Ye, "First direct measurement of sub-nanosecond polarization switching in ferroelectric hafnium zirconium oxide" in *2019 IEEE International Electron Devices Meeting (IEDM)* (IEEE, 2019), pp. 15.2.1–15.2.4.

78. M. Si, X. Lyu, P. R. Shrestha, X. Sun, H. Wang, K. P. Cheung, P. D. Ye, Ultrafast measurements of polarization switching dynamics on ferroelectric and anti-ferroelectric hafnium zirconium oxide. *Appl. Phys. Lett.* **115**, 072107 (2019). doi:10.1063/1.5098786

79. X. Lyu, M. Si, P. R. Shrestha, J. P. Campbell, K. P. Cheung, P. D. Ye, "Record fast polarization switching observed in ferroelectric hafnium oxide crossbar arrays" in *2020 IEEE Silicon Nanoelectronics Workshop (SNW)* (IEEE, 2020), pp. 7–8.

80. H. Wang, Z. R. Liu, H. Y. Yoong, T. R. Paudel, J. X. Xiao, R. Guo, W. N. Lin, P. Yang, J. Wang, G. M. Chow, T. Venkatesan, E. Y. Tsymbal, H. Tian, J. S. Chen, Direct observation of room-temperature out-of-plane ferroelectricity and tunneling electroresistance at the two-dimensional limit. *Nat. Commun.* **9**, 3319 (2018). doi:10.1038/s41467-018-05662-y Medline

81. V. Garcia, S. Fusil, K. Bouzehouane, S. Enouz-Vedrenne, N. D. Mathur, A. Barthélémy, M. Bibes, Giant tunnel electroresistance for non-destructive readout of ferroelectric states. *Nature* **460**, 81–84 (2009). doi:10.1038/nature08128 Medline

82. S. Yuan, X. Luo, H. L. Chan, C. Xiao, Y. Dai, M. Xie, J. Hao, Room-temperature ferroelectricity in $MoTe_2$ down to the atomic monolayer limit. *Nat. Commun.* **10**, 1775 (2019). doi:10.1038/s41467-019-09669-x Medline

83. Q. H. Qin, L. Äkäslompolo, N. Tuomisto, L. Yao, S. Majumdar, J. Vijayakumar, A. Casiraghi, S. Inkinen, B. Chen, A. Zugarramurdi, M. Puska, S. van Dijken, Resistive switching in all-oxide ferroelectric tunnel junctions with ionic interfaces. *Adv. Mater.* **28**, 6852–6859 (2016). doi:10.1002/adma.201504519 Medline

84. H. Kohlstedt, A. Petraru, K. Szot, A. Rüdiger, P. Meuffels, H. Haselier, R. Waser, V. Nagarajan, Method to distinguish ferroelectric from nonferroelectric origin in case of resistive switching in ferroelectric capacitors. *Appl. Phys. Lett.* **92**, 062907 (2008). doi:10.1063/1.2841917

85. W. Lü, C. Li, L. Zheng, J. Xiao, W. Lin, Q. Li, X. R. Wang, Z. Huang, S. Zeng, K. Han, W. Zhou, K. Zeng, J. Chen, W. Ariando, W. Cao, T. Venkatesan, Multi-nonvolatile state resistive switching arising from ferroelectricity and oxygen vacancy migration. *Adv. Mater.* **29**, 1606165 (2017). doi:10.1002/adma.201606165

86. M. Qian, I. Fina, M. C. Sulzbach, F. Sánchez, J. Fontcuberta, Synergetic electronic and ionic contributions to electroresistance in ferroelectric capacitors. *Adv. Electron. Mater.* **5**, 1800646 (2019). doi:10.1002/aelm.201800646

87. Z. Wen, D. Wu, Ferroelectric tunnel junctions: Modulations on the potential barrier. *Adv. Mater.* **32**, e1904123 (2020). Medline

88. V. Garcia, M. Bibes, Ferroelectric tunnel junctions for information storage and processing. *Nat. Commun.* **5**, 4289 (2014). doi:10.1038/ncomms5289 Medline

89. M. C. Sulzbach, S. Estandía, X. Long, J. Lyu, N. Dix, J. Gàzquez, M. F. Chisholm, F. Sánchez, I. Fina, J. Fontcuberta, Unraveling ferroelectric polarization and ionic contributions to electroresistance in epitaxial $Hf_{0.5}Zr_{0.5}O_2$ tunnel junctions. *Adv. Electron. Mater.* **6**, 1900852 (2020). doi:10.1002/aelm.201900852

90. M. C. Sulzbach, S. Estandía, J. Gàzquez, F. Sánchez, I. Fina, J. Fontcuberta, Blocking of conducting channels widens window for ferroelectric resistive switching in interface-engineered $Hf_{0.5}Zr_{0.5}O_2$ tunnel devices. *Adv. Funct. Mater.* **30**, 2002638 (2020). doi:10.1002/adfm.202002638

91. B. Max, M. Pešic, S. Slesazeck, T. Mikolajick, Interplay between ferroelectric and resistive switching in doped crystalline HfO_2. *J. Appl. Phys.* **123**, 134102 (2018). doi:10.1063/1.5015985

92. V. Mikheev, A. Chouprik, Y. Lebedinskii, S. Zarubin, A. M. Markeev, A. V. Zenkevich, D. Negrov, Memristor with a ferroelectric HfO_2 layer: In which case it is a ferroelectric tunnel junction. *Nanotechnology* **31**, 215205 (2020). doi:10.1088/1361-6528/ab746d Medline

93. M. Materano, P. D. Lomenzo, A. Kersch, M. H. Park, T. Mikolajick, U. Schroeder, Interplay between oxygen defects and dopants: Effect on structure and performance of HfO_2-based ferroelectrics. *Inorg. Chem. Front.* **8**, 2650–2672 (2021). doi:10.1039/D1QI00167A

94. R. Waser, R. Dittmann, G. Staikov, K. Szot, Redox-based resistive switching memories – Nanoionic mechanisms, prospects, and challenges. *Adv. Mater.* **21**, 2632–2663 (2009). doi:10.1002/adma.200900375

95. D. S. Jeong, R. Thomas, R. S. Katiyar, J. F. Scott, H. Kohlstedt, A. Petraru, C. S. Hwang, Emerging memories: Resistive switching mechanisms and current status. *Rep. Prog. Phys.* **75**, 076502 (2012). doi:10.1088/0034-4885/75/7/076502 Medline

96. H.-S. P. Wong, H.-Y. Lee, S. Yu, Y.-S. Chen, Y. Wu, P.-S. Chen, B. Lee, F. T. Chen, M.-J. Tsai, Metal–oxide RRAM. *Proc. IEEE* **100**, 1951–1970 (2012). doi:10.1109/JPROC.2012.2190369

97. A. Chanthbouala, A. Crassous, V. Garcia, K. Bouzehouane, S. Fusil, X. Moya, J. Allibe, B. Dlubak, J. Grollier, S. Xavier, C. Deranlot, A. Moshar, R. Proksch, N. D. Mathur, M. Bibes, A. Barthélémy, Solid-state memories based on ferroelectric tunnel junctions. *Nat. Nanotechnol.* **7**, 101–104 (2011). doi:10.1038/nnano.2011.213 Medline

98. M. H. Park, T. Schenk, S. Starschich, C. M. Fancher, H. J. Kim, U. Böttger, C. S. Hwang, A. Toriumi, X. Tian, U. Schroeder, "Effect of surface/interface energy and stress on the ferroelectric properties" in *Ferroelectricity in Doped Hafnium Oxide: Materials, Properties and Devices*, U. Schroeder, C. Hwang, H. Funakubo, Eds. (Elsevier, 2019), pp. 145–172.

99. M. H. Park, Y. H. Lee, T. Mikolajick, U. Schroeder, C. S. Hwang, Thermodynamic and kinetic origins of ferroelectricity in fluorite structure oxides. *Adv. Electron. Mater.* **5**, 1800522 (2019). doi:10.1002/aelm.201800522

100. C. Künneth, R. Batra, G. A. Rossetti, R. Ramprasad, A. Kersch, "Thermodynamics of phase stability and ferroelectricity from first principles" in *Ferroelectricity in Doped Hafnium Oxide: Materials, Properties and Devices*, U. Schroeder, C. Hwang, H. Funakubo, Eds. (Elsevier, 2019), pp. 245–289.

101. H. J. Kim, Y. An, Y. C. Jung, J. Mohan, J. G. Yoo, Y. I. Kim, H. Hernandez-Arriaga, H. S. Kim, J. Kim, S. J. Kim, Low-thermal budget fluorite-structure ferroelectrics for future electronic device applications. *Phys. Status Solidi RRL* **15**, 2100028 (2021). doi:10.1002/pssr.202100028

102. T. Mikolajick, U. Schroeder, Ferroelectricity in bulk hafnia. *Nat. Mater.* **20**, 718–719 (2021). doi:10.1038/s41563-020-00914-z Medline

103. C. Kittel, Theory of antiferroelectric crystals. *Phys. Rev.* **82**, 729–732 (1951). doi:10.1103/PhysRev.82.729

104. M. H. Park, C. S. Hwang, Fluorite-structure antiferroelectrics. *Rep. Prog. Phys.* **82**, 124502 (2019). doi:10.1088/1361-6633/ab49d6 Medline

105. K. M. Rabe, “Antiferroelectricity in oxides: A reexamination” in *Functional Metal Oxides*, S. B. Ogale, T. V. Venkatesan, M. G. Blamire, Eds. (Wiley, 2013), pp. 221–244.

106. T. Shimizu, Y. Tashiro, T. Mimura, T. Kiguchi, T. Shiraishi, T. J. Konnno, O. Sakata, H. Funakubo, Electric-field-induced ferroelectricity in 5%Y-doped $Hf_{0.5}Zr_{0.5}O_2$: Transformation from the paraelectric tetragonal phase to the ferroelectric orthorhombic phase. *Phys. Status Solidi RRL* **15**, 2000589 (2021). doi:10.1002/pssr.202000589

107. Y. Zheng, C. Zhong, Y. Zheng, Z. Gao, Y. Cheng, Q. Zhong, C. Liu, Y. Wang, R. Qi, R. Huang, H. Lyu, “In-situ atomic visualization of structural transformation in $Hf_{0.5}Zr_{0.5}O_2$ ferroelectric thin film: from nonpolar tetragonal phase to polar orthorhombic phase” in *2021 Symposium on VLSI Technology* (IEEE, 2021), pp. T16–3.

108. S. Lombardo, C. Nelson, K. Chae, S. Reyes-Lillo, M. Tian, N. Tasneem, Z. Wang, M. Hoffmann, D. Triyoso, S. Consiglio, K. Tapily, R. Clark, G. Leusink, K. Cho, A. Kummel, J. Kacher, A. I. Khan, “Atomic-scale imaging of polarization switching in an (anti)ferroelectric memory material: Zirconia (ZrO_2)” in *2020 IEEE Symposium on VLSI Technology* (IEEE, 2020), pp. 1–2.

109. S. D. Hyun, H. W. Park, M. H. Park, Y. H. Lee, Y. B. Lee, B. Y. Kim, H. H. Kim, B. S. Kim, C. S. Hwang, Field-induced ferroelectric $Hf_{1-x}Zr_xO_2$ thin films for high-κ dynamic random access memory. *Adv. Electron. Mater.* **6**, 2000631 (2020). doi:10.1002/aelm.202000631

110. T. S. Böscke, S. Teichert, D. Bräuhaus, J. Müller, U. Schröder, U. Böttger, T. Mikolajick, Phase transitions in ferroelectric silicon doped hafnium oxide. *Appl. Phys. Lett.* **99**, 112904 (2011). doi:10.1063/1.3636434

111. S. Mueller, J. Mueller, A. Singh, S. Riedel, J. Sundqvist, U. Schroeder, T. Mikolajick, Incipient ferroelectricity in Al-doped HfO_2 thin films. *Adv. Funct. Mater.* **22**, 2412–2417 (2012). doi:10.1002/adfm.201103119

112. M. H. Park, C. Chung, T. Schenk, C. Richter, M. Hoffmann, S. Wirth, J. L. Jones, T. Mikolajick, U. Schroeder, Origin of temperature-dependent ferroelectricity in Si-doped HfO_2. *Adv. Electron. Mater.* **4**, 1700489 (2018). doi:10.1002/aelm.201700489

113. P. D. Lomenzo, S. Slesazeck, T. Mikolajick, U. Schroeder, “Thickness scaling of AFERAM ZrO_2 capacitors with high cycling endurance and low process temperature” in *2020 IEEE International Memory Workshop (IMW)* (IEEE, 2020), pp. 1–4.

114. X. Luo, K. Toprasertpong, M. Takenaka, S. Takagi, Antiferroelectric properties of ZrO_2 ultra-thin films prepared by atomic layer deposition. *Appl. Phys. Lett.* **118**, 232904 (2021). doi:10.1063/5.0051068

115. R. Batra, T. D. Huan, J. L. Jones, G. Rossetti Jr., R. Ramprasad, Factors favoring ferroelectricity in hafnia: A first-principles computational study. *J. Phys. Chem. C* **121**, 4139–4145 (2017). doi:10.1021/acs.jpcc.6b11972

116. B. J. Kooi, B. Noheda, Ferroelectric chalcogenides—Materials at the edge. *Science* **353**, 221–222 (2016). doi:10.1126/science.aaf9081 Medline

117. D. G. Schlom, L.-Q. Chen, C. J. Fennie, V. Gopalan, D. A. Muller, X. Pan, R. Ramesh, R. Uecker, Elastic strain engineering of ferroic oxides. *MRS Bull.* **39**, 118–130 (2014). doi:10.1557/mrs.2014.1

118. K. Yasuda, X. Wang, K. Watanabe, T. Taniguchi, P. Jarillo-Herrero, Stacking-engineered ferroelectricity in bilayer boron nitride. *Science* **372**, 1458–1462 (2021). doi:10.1126/science.abd3230 Medline

119. M. Vizner Stern, Y. Waschitz, W. Cao, I. Nevo, K. Watanabe, T. Taniguchi, E. Sela, M. Urbakh, O. Hod, M. Ben Shalom, Interfacial ferroelectricity by van der Waals sliding. *Science* **372**, 1462–1466 (2021). doi:10.1126/science.abe8177 Medline

120. Z. Zheng, Q. Ma, Z. Bi, S. de la Barrera, M.-H. Liu, N. Mao, Y. Zhang, N. Kiper, K. Watanabe, T. Taniguchi, J. Kong, W. A. Tisdale, R. Ashoori, N. Gedik, L. Fu, S.-Y. Xu, P. Jarillo-Herrero, Unconventional ferroelectricity in moiré heterostructures. *Nature* **588**, 71–76 (2020). doi:10.1038/s41586-020-2970-9 Medline

121. K. Chang, J. Liu, H. Lin, N. Wang, K. Zhao, A. Zhang, F. Jin, Y. Zhong, X. Hu, W. Duan, Q. Zhang, L. Fu, Q.-K. Xue, X. Chen, S.-H. Ji, Discovery of robust in-plane ferroelectricity in atomic-thick SnTe. *Science* **353**, 274–278 (2016). doi:10.1126/science.aad8609 Medline

122. N. Higashitarumizu, H. Kawamoto, C.-J. Lee, B.-H. Lin, F.-H. Chu, I. Yonemori, T. Nishimura, K. Wakabayashi, W.-H. Chang, K. Nagashio, Purely in-plane ferroelectricity in monolayer SnS at room temperature. *Nat. Commun.* **11**, 2428 (2020). doi:10.1038/s41467-020-16291-9 Medline

123. Z. Fei, W. Zhao, T. A. Palomaki, B. Sun, M. K. Miller, Z. Zhao, J. Yan, X. Xu, D. H. Cobden, Ferroelectric switching of a two-dimensional metal. *Nature* **560**, 336–339 (2018). doi:10.1038/s41586-018-0336-3 Medline

124. F. Xue, W. Hu, K. Lee, L. Lu, J. Zhang, H. Tang, A. Han, W. Hsu, S. Tu, W. Chang, C. Lien, J. He, Z. Zhang, L. Li, X. Zhang, Room-temperature ferroelectricity in hexagonally layered α-In_2Se_3 nanoflakes down to the monolayer limit. *Adv. Funct. Mater.* **28**, 1803738 (2018). doi:10.1002/adfm.201803738

125. L. You, F. Liu, H. Li, Y. Hu, S. Zhou, L. Chang, Y. Zhou, Q. Fu, G. Yuan, S. Dong, H. J. Fan, A. Gruverman, Z. Liu, J. Wang, In-plane ferroelectricity in thin flakes of van der Waals hybrid perovskite. *Adv. Mater.* **30**, e1803249 (2018). doi:10.1002/adma.201803249 Medline

126. F. Liu, L. You, K. L. Seyler, X. Li, P. Yu, J. Lin, X. Wang, J. Zhou, H. Wang, H. He, S. T. Pantelides, W. Zhou, P. Sharma, X. Xu, P. M. Ajayan, J. Wang, Z. Liu, Room-temperature ferroelectricity in $CuInP_2S_6$ ultrathin flakes. *Nat. Commun.* **7**, 12357 (2016). doi:10.1038/ncomms12357 Medline

127. A. V. Bune, V. M. Fridkin, S. Ducharme, L. M. Blinov, S. P. Palto, A. V. Sorokin, S. G. Yudin, A. Zlatkin, Two-dimensional ferroelectric films. *Nature* **391**, 874–877 (1998). doi:10.1038/36069

128. D. Ji, S. Cai, T. R. Paudel, H. Sun, C. Zhang, L. Han, Y. Wei, Y. Zang, M. Gu, Y. Zhang, W. Gao, H. Huyan, W. Guo, D. Wu, Z. Gu, E. Y. Tsymbal, P. Wang, Y. Nie, X. Pan, Freestanding crystalline oxide perovskites down to the monolayer limit. *Nature* **570**, 87–90 (2019). doi:10.1038/s41586-019-1255-7 Medline

129. P. Gao, Z. Zhang, M. Li, R. Ishikawa, B. Feng, H.-J. Liu, Y.-L. Huang, N. Shibata, X. Ma, S. Chen, J. Zhang, K. Liu, E.-G. Wang, D. Yu, L. Liao, Y.-H. Chu, Y. Ikuhara, Possible

absence of critical thickness and size effect in ultrathin perovskite ferroelectric films. *Nat. Commun.* **8**, 15549 (2017). doi:10.1038/ncomms15549 Medline

130. A. Chernikova, M. Kozodaev, A. Markeev, D. Negrov, M. Spiridonov, S. Zarubin, O. Bak, P. Buragohain, H. Lu, E. Suvorova, A. Gruverman, A. Zenkevich, Ultrathin $Hf_{0.5}Zr_{0.5}O_2$ ferroelectric films on Si. *ACS Appl. Mater. Interfaces* **8**, 7232–7237 (2016). doi:10.1021/acsami.5b11653 Medline

131. H. Lee, D. H. Choe, S. Jo, J.-H. Kim, H. H. Lee, H. J. Shin, Y. Park, S. Kang, Y. Cho, S. Park, T. Moon, D. Eom, M. Leem, Y. Kim, J. Heo, E. Lee, H. Kim, Unveiling the origin of robust ferroelectricity in sub-2 nm hafnium zirconium oxide films. *ACS Appl. Mater. Interfaces* **13**, 36499–36506 (2021). doi:10.1021/acsami.1c08718 Medline

132. Z. Gao, Y. Luo, S. Lyu, Y. Cheng, Y. Zheng, Q. Zhong, W. Zhang, H. Lyu, Identification of ferroelectricity in a capacitor with ultra-thin (1.5-nm) $Hf_{0.5}Zr_{0.5}O_2$ film. *IEEE Electron Device Lett.* **42**, 1303–1306 (2021). doi:10.1109/LED.2021.3097332